Master Thesis

Deployment of an Ultra-Wideband Indoor Positioning System

Stefan Hinteregger

_____

Signal Processing and Speech Communication
Graz University of Technology
Head: O. Univ.-Prof. Dipl.-Ing. Dr. techn. Gernot Kubin

in Cooperation with CISC Semiconductor Design+Consulting GmbH, Klagenfurt

Supervisor: Assoc.-Prof. Dipl.-Ing. Dr. Klaus Witrisal

Graz, December 2011

Kurzfassung

Im Gegensatz zu gebräuchlichen Navigationssystemen wie GPS, ermöglichen aufgrund der Unterscheidbarkeit der einzelnen Mehrwegekomponenten Impulsradio UWB Signale, hochpräzise Enfernungs- und Positionsmessungen auch in Räumen. Das Hauptziel dieser Arbeit ist die Abschätzung der möglichen Positionierungsgüte eines Innenraum UWB-Positionierungssystem in einem spezifischen Anwendungsszenario.

Dafür wurde ein kohärenter Empfänger zur Kanalschätzung entwickelt, welcher mit einem zuvor entwickelten Sender arbeitet, der den IEEE 802.15.4a Standard implementiert. Mit den zuvor berechneten Kanalimpulsantworten wird anschließend die Entfernung zwischen Sender und Empfänger geschätzt aus der Laufzeit der ersten, direkten Mehrwegekomponente.

Zur Bestimmung der Entfernungs- und Positionierungsgüte, wurden Messungen in zwei Räumen durchgeführt, einem Hörsaal sowie einem Büroraum. In beiden Räumen wurde die Entfernung zu sechs Basisstationen geschätzt, um mittels einer iterativen Methode der kleinsten Quadrate die Position des Senders zu estimieren. Folglich konnten Gütemaße der Enfernungs- und Positionierungschätzung berechnet werden. Des weiteren wurden wichtige Parameter der Mehrwegeausbreitung berechnet um die beiden Räume miteinander zu vergleichen.

Abschließend wurde ein Vergleich mit einem Simulationsprogramm durchgeführt um dieses zu validieren.

Abstract

In contrast to common navigation systems as GPS, Impulse Radio UWB-signals enable high-accuracy ranging and positioning indoors, due to the resolvability of the individual multipath components. The aim of this thesis is to evaluate the potential positioning performance of an indoor UWB-positioning system in a specific application scenario.

For this purpose a coherent receiver for channel estimation has been developed, which is used with a previously developed transmitter for the IEEE 802.15.4a standard. After obtaining the channel impulse response, ranging is performed with a jump-back and search-forward leading edge detector.

To be able to evaluate the ranging and positioning performance, measurements in two different environments have been made; a lecture hall and an office room. To gather position estimates, the distances to six different base stations have been calculated in each room. These range estimates have afterwards been combined by an iterative least-squares positioning algorithm. Furthermore important parameters of multipath propagation have been calculated to compare the two environments.

Finally a comparison to a simulation framework called U-SPOT is presented to validate it.

Deutsche Fassung:

EIDESSTATTLICHE ERKLÄRUNG

Ich erkläre an Eides statt, dass ich die vorliegende Arbeit selbstständig verfasst, andere als die angegebenen Quellen/Hilfsmittel nicht benutzt, und die den benutzten Quellen wörtlich und inhaltlich entnommenen Stellen als solche kenntlich gemacht habe.

Graz,am ....

                                                                      (Unterschrift)

Englische Fassung:

STATUTORY DECLARATION

I declare that I have authored this thesis independently, that I have not used other than the declared sources / resources, and that I have explicitly marked all material which has been quoted either literally or by content from the used sources.

....

date   (signature)

Acknowledgements

This thesis was written at the Signal Processing and Speech Communication (SPSC) Laboratory at the University of Technology Graz in the year 2011.

I would like to thank my supervisor Klaus Witrisal for supporting me with inspiring suggestions during the whole process of this thesis. Moreover I want to thank the complete staff at the SPSC institute, especially the Wireless Communication group for the pleasant working environment.

Furthermore I like to thank Josef Preishuber-Pflügl and the company CISC Semiconductor Design+Consulting GmbH for making this work possible.

A special thanks to my colleague Erik Leitinger for all the fruitful discussions during our study time at TU Graz.

Finally I like to thank my girlfriend, my family and all friends for supporting me throughout this work.

Thank you.

Graz, December 2011 Stefan Hinteregger

Contents

List of Figures

List of Tables

List of Abbreviations & Symbols

Abbreviations

BPF	Band-Pass Filter
BPM	Burst Position Modulation
BPSK	Binary Phase Shift Keying
BS	Base Station
CEP	Circular Error Probability
CEPT	European Conference of Postal and Telecommunication Administrations
CIR	Channel Impulse Response
DSO	Digital Sampling Oscilloscope
FCC	Federal Communication Commission
FPGA	Field Programmable Gate Array
GSM	Global System for Mobile Communication
IPI	Inter-Pulse Interference
ISM-band	Industrial, Scientific and Medical band
JBSF	Jump-Back and Search-Forward
LNA	Low-Noise-Amplifier
LOS	Line Of Sight
LPF	Low-Pass Filter
LS	Least Squares
MAE	Mean Absolute Error
MGT	Multi-Gigabit Transceiver
MPC	Multipath Component
NLOS	Non Line Of Sight
pdp	power delay profile
PHR	PHY Header
PHY	Physical Layer
PPDU	PHY Protocol Data Unit
PRF	Pulse Repetition Frequency
PSD	Power Spectral Density
RX	Receiver
SFD	Start of Frame Delimiter

SHR	Synchronization Header
SYNC	Synchronization
TOA	Time Of Arrival
TX	Transmitter
U-SPOT	UWB System-Level Simulator for Positioning and Tracking
UWB	Ultra-Wide Band
W-LAN	Wireless Local Area Network

Variables

$\bar{\tau}$	mean excess delay
β	Roll-Off-Factor
η	pathloss exponent
$\hat{\tau}_{\mathrm{LOS}}$	estimated arrival time of LOS component
$\hat{d}$	estimated distance between TX and RX
$\hat{f}_{\mathrm{c,low}}$	Estimated mirrored carrier frequency
$\hat{f}_{\mathrm{c}}$	Estimated carrier frequency
$\hat{h}[k]$	Estimated Channel Impulse Response
$\Phi(\tau)$	Normalized Cross Correlation
τ_{rms}	rms delay spread
$\boldsymbol{\delta}_{\mathrm{L}}$	Delta Function with length L
$\boldsymbol{c}_{\mathrm{i}}$	Preamble Code Sequence
$\boldsymbol{D}$	Despreading Matrix
$\boldsymbol{f}_{\mathrm{c,low}}$	Mirror Center Frequencies
$\boldsymbol{S}_{\mathrm{i}}$	Preamble Symbol
B	Bandwidth
e_{pos}	positioning error
E_{p}	Energy of the Pulse
e_{rang}	ranging error
E_{r}	Energy of the Reference Pulse
e_{x}	positioning error in x-direction
e_{y}	positioning error in y-direction
f'_{s}	Sampling frequency after zero-padding
f_{c}	Center Frequency
f_{chip}	peak PRF
f_{s}	Sampling Frequency
$h_{\mathrm{l}}(t)$	Complex baseband channel
$K_{\mathrm{los,dB}}$	Ricean K-factor for the LOS component
L	Spreading Factor
N'_{c}	Number of samples for one spreaded preamble bit sampled with f'_{s}
N'_{samples}	Number of samples when sampled with f'_{s}

N_{code}	Number of code bits
N_{samples}	Number of samples when sampled with f_{s}
N_{sfd}	Number of Symbols per Preamble
N_{sync}	Number of Symbols per Preamble
$p(t)$	Transmitted Pulse
PL	pathloss
$r(t)$	Received signal in passband representation
r_{d}	reverberation distance
$r_{\text{l}}(t)$	Received signal in baseband representation
$rrc(t)$	Root Raised Cosine Pulse, reference pulse
S	log-normal shadowing random variable
$s_{\text{l}}(t)$	Sent signal in baseband representation
T_{s}'	Sampling Time after Zero Padding
T_{1pr}	Duration of one preamble symbol
T_{chip}	Chip Duration
T_{pr}	Duration of the preamble
T_{p}	Pulse Duration
T_{rrc}	Duration of the RRC Filter
T_{s}	Sampling Time
T_{w}	Main Lobe Width
v_{c}	speed of light

Chapter 1

Introduction

1.1   Motivation

Wireless devices become more important in our life every day. Especially context aware applications are used increasingly often in modern communications. One important aspect of the context we live in, is the position. Therefore ranging and positioning are interesting research areas. Common navigation systems like GPS or GALILEO are only reliable outdoor since they need a line of sight between the transmitter and the receiver. The positioning error of such systems ranges from 1 to 10 m.

Many indoor applications need an accuracy of approximately 1 m. Examples are the tracking of goods and items in logistics, exhibit/museums commentary, hazard warnings, location based office services, in-building people tracking and pedestrian route guidance.

For indoor ranging and positioning Ultra-wideband signals (UWB) are a candidate to deliver an accuracy below 1 m. An UWB signal has either a fractional bandwidth greater than 0.2 or its bandwidth exceeds 500 MHz. Especially Impulse Radio UWB (IR-UWB) signals where the high bandwidth is produced by a train of ultra-short pulses are used. In indoor scenarios, lots of reflections occur, hence many multipath components (MPC) arrive at the receiver. Due to the high bandwidth, these MPCs do not overlap in comparison to narrowband signals, hence the individual MPCs can be resolved. As the bandwidth is indirect proportional to the temporal resolution and therefore lies in the dimension of nanoseconds, accurate ranging is possible.

The IEEE 802.15.4a [IEE07b] standard defines an IR-UWB transmission protocol. The standard enables not only for indoor precision ranging with a synchronization preamble,

but also for data communication. During data communication burst position modulation (BPM) and binary phase shift keying (BPSK) is implemented to encode two bits. To make use of the BPSK bit, a coherent receiver has to be used. A rake receiver for example needs an accurate channel estimate which can be obtained from the preamble part of the standard. The BPM bit can also be encoded by a low-complexity non-coherent RX.

Three different techniques are used for positioning. One possibility is to exploit the angle of arrival (AoA). The second one is to utilize the received signal strength (RSS) which decreases with the square of the distance while the third alternative measures the time of arrival (TOA) of the received signal. For simple TOA a calibration measurement or a synchronized clock is needed. One way out is to use time difference of arrival (TDOA) which needs one base station more than TOA for positioning. To obtain a position estimate with TOA in a 2-D environment, three range estimates to three base stations are needed.

TOA ranging with IR-UWB signals is a well-investigated field, hence lots of literature exist. The interested reader should refer to [DCF$^+$09] which presents an overview of the topic.

During previous projects at Graz University of Technology in collaboration with CISC Semiconductor GmbH and Vienna University of Technology, a demonstrator, which implements the IEEE 802.15.4a standard has been developed [Gig10], [Buc08]. With this demonstrator measurements have been performed and the ranging capabilities with a low-complexity energy detection receiver [Gei09], [Til10] and a coherent receiver [Gig10] have been analysed.

The aim of this thesis is to evaluate the potential performance of an indoor positioning system in specific application scenarios. These scenarios are a lecture hall, since the geometry of such a room is interesting, and an office room. For this purpose a coherent receiver has been developed and measurements with the previously mentioned demonstrator were performed.

1.2   Outline

This report is organized in the following way: In Chapter 2, the IEEE 802.15.4a standard is introduced. This chapter presents only a short overview of the standard and explains mainly the parts that have been needed for this work.

Chapter 3 analyses the sent signal of the demonstrator and the received signal of a base station. Due to restrictions of the measurement equipment, a sampling frequency close to half the carrier frequency has been used, hence aliasing occurrs. A coherent receiver which is able to cope with this aliasing is developed, to estimate the channel impulse response.

The first part of Chapter 4 gives a brief summary of the ranging system, a threshold based leading edge detection. The second part of this chapter outlines an iterative least squares algorithm that was used for positioning.

All the measurements, which were done in two different environments, as well as the ranging and positioning results can be seen in Chapter 5. Important parameters of multipath propagation are estimated to compare the two environments.

In Chapter 6 the obtained channel impulse responses are embedded in a previously developed simulator framework (U-SPOT [Gig10]) to validate the simulator and compare the results of the simulation and the measurements.

Chapter 2

Overview of the IEEE 802.15.4a Standard

The IEEE 802.15.4a [IEE07b] standard is an amendment to the IEEE 802.15.4 [IEE06] standard with the intention of adding precise ranging, extended range, enhanced robustness and mobility. Therfore two additional Physical Layers (PHY) are defined:

- Ultra-wide band (UWB) PHY at 3GHz to 10GHz and below 1GHz

- Chirp spread spectrum PHY

In the next part of this chapter, the UWB-PHY will be introduced. Note that this is just a short overview and the interested reader shall directly consult the standard [IEE07b].

2.1   Basics of the Ultra-wide Band Physical Layer

The UWB-PHY defines sixteen channels which are divided into three sub-bands (Table 2.1). An UWB-compliant device shall at least implement one of the three mandatory channels 0, 3 or 9 in Table 2.1. Another aspect is that the bandwidth varies for different channels, where higher bandwidth enables more accurate ranging [Gig10].

2.1.1   Packet Structure

In Figure 2.1 the structure of one PHY protocol data unit (PPDU) can be seen. It consists of three major parts: the Synchronization Header (SHR) preamble, the Physical Header

Channel Number	Center frequency f_c [MHz]	Bandwidth B [MHz]	Sub-band
0	499.2	499.2	Sub-GHz
1	3494.4	499.2	Low-band
2	3993.6	499.2	Low-band
3	4492.8	499.2	Low-band
4	3993.6	1331.2	Low-band
5	6489.6	499.2	High-band
6	6988.8	499.2	High-band
7	6489.6	1081.6	High-band
8	7488.0	499.2	High-band
9	7987.2	499.2	High-band
10	8486.4	499.2	High-band
11	7987.2	1331.2	High-band
12	8985.6	499.2	High-band
13	9484.8	499.2	High-band
14	9984.0	499.2	High-band
15	9484.8	1354.97	High-band

Table 2.1: UWB-PHY-channels [IEE07b]

		Bits	Octets
		19	variable
Preamble	SFD	PHR (see 6.8a.7)	PSDU
SHR		PHR	PHY payload

Figure 2.1: Packet Structure of an UWB frame [IEE07b] (©IEEE 2007)

(PHR) and the PHY payload.

During transmitting the SHR preamble, which is transmitted first in time, the standard defines Binary Phase Shift Keying (BPSK) as coding scheme where one bit can be encoded. The PHR is sent after the SHR and contains information about the frame length, the transmission rate, ranging and the preamble. For the PHR BPSK and Burst Position Modulation (BPM) can be used, hence two bits can be encoded. At the end the PHY payload is sent with BPSK and BPM at a variable rate. As for ranging only the SHR is used, this part of the frame will be described in the next section.
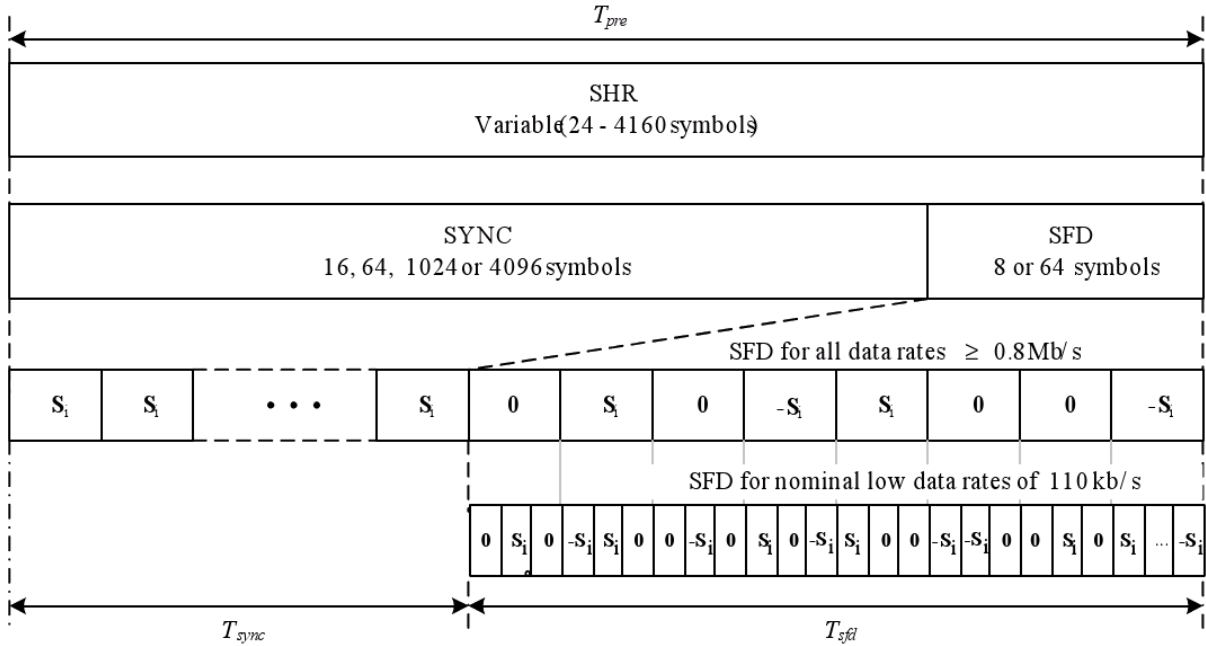
Figure 2.2: Packet Structure of the SHR preamble [IEE07b] (©IEEE 2007)

2.2 Synchronization Header Preamble

In Figure 2.2 it can be seen that the SHR preamble is subdivided into two distinct portions: the Synchronization (SYNC) part and the Start of Frame Delimiter (SFD) part.

If an UWB-compliant device wants to send on a specific channel (0-15, see Table 2.1) it also has to use a preamble code to distinguish the channels further. This preamble code is constructed out of a ternary alphabet $-1, 0, 1$ with a length of N_{code} 31 or 127 bits. All preamble codes have perfect periodic autocorrelation properties [IEE07b] and are therefore used in the UWB PHY. The length 31 codes are shown in Table 2.2, where a - means -1 and a + means +1 respectively. The third column indicates a set of channels for which this code can be used. This restriction is due to the fact, that only codes with the lowest cross-correlation are used within the same channel.

From here on, the following notation is used: column vectors and matrices are denoted by lower and upper case boldface symbols, respectively. Estimated values are represented by hats.

After choosing a code sequence, a preamble symbol $\boldsymbol{S}_{\text{i}}$ is constructed by spreading the code sequence $\boldsymbol{c}_{\text{i}}$ with $\boldsymbol{\delta}_{\text{L}}$, which is a vector with a 1 at the first position and $(L-1)$ zeros

Code Index	Code Sequence	Channel Number
1	-0000+0-0+++0+-000+-+++00-+0-00	0, 1, 8, 12
2	0+0+-0+0+000-++0-+—00+00++000	0, 1, 8, 12
3	-+0++000-+-++00++0+00-0000-0+0-	2, 5, 9, 13
4	0000+-00-00-+++++0+-+000+0-0++0-	2, 5, 9, 13
5	-0+-00+++-+000-+0+++0-0+0000-00	3, 6, 10, 14
6	++00+00—+-0++-000+0+0-+0+0000	3, 6, 10, 14
7	+0000+-0+0+00+000+0++—0-+00-+	4, 7, 11, 15
8	0+00-0-0++0000—+00-+0++-++0+00	4, 7, 11, 15

Table 2.2: Preamble Codes with length 31 [IEE07b]

Channel number	Code Length	L	N_sync	N_sfd
0:15	31	16		
0:3,5:6,8:10,12:14	31	64	16,64,1024,4096	8,64
0:15	127	4		

Table 2.3: Parameters for SHR preamble [IEE07b]

afterwards. This operation is described in Equation 2.1, where the operator $\otimes$ indicates the Kronecker product.

$$\boldsymbol{S}_\mathrm{i} = \boldsymbol{c}_\mathrm{i} \otimes \boldsymbol{\delta}_\mathrm{L} \tag{2.1}$$

After obtaining one preamble symbol, the whole preamble, which is the SYNC part of the SHR preamble, is simply the repetition of one preamble symbol N_sync times. The SFD part, which is added to establish frame timing, is produced by sending N_sfd repetitions of one preamble symbol modulated with the SFD code which can be seen in Figure 2.2. The possible values for L, N_sync and N_sfd can be seen in Table 2.3.

2.3   Baseband Pulse Shaping

The standard defines a root raised cosine UWB-reference pulse $rrc(t)$

$$rrc(t) = \frac{4\beta}{\pi\sqrt{T_\mathrm{p}}} \frac{\cos[(1+\beta)\frac{\pi t}{T_\mathrm{p}}] + \frac{\sin[(1-\beta)\frac{\pi t}{T_\mathrm{p}}]}{4\beta\frac{t}{T_\mathrm{p}}}}{1 - (4\beta\frac{t}{T_\mathrm{p}})^2} \tag{2.2}$$

Channel number	T_p in [ns]	T_w in [ns]
0:3, 5:6, 8:10, 12:14	2.00	0.5
7	0.92	0.2
4,11	0.75	0.2
15	0.74	0.2

Table 2.4: Pulse Duration and Main Lobe Width [IEE07b]

where $\beta = 0.6$ is the roll-off factor, T_p is the pulse duration. Because this pulse is non causal it is not possible to produce such a pulse in practice. Therefore the transmitted pulse $p(t)$ for the UWB-PHY is constrained by its normalized cross correlation to the reference pulse.

$$\Phi(\tau) = \frac{1}{\sqrt{E_\text{r} E_\text{p}}} \text{Re}\left\{ \int_{-\infty}^{\infty} rrc(t)p^*(t+\tau)dt \right\} \tag{2.3}$$

In the above equation E_p and E_r are the energies of the transmitted pulse $p(t)$ and the reference pulse $rrc(t)$. To check if a pulse is standard compliant one has to calculate the normalized cross correlation and test if the following constraints hold:

- the peak of the main lobe has to be greater than 0.8 for at least T_w

- any sidelobe shall be no greater than 0.3

The pulse duration T_p is channel dependent because it is indirect proportional to the used bandwidth and can be seen in Table 2.4 as well as the main lobe width T_w. In the middle of Figure 2.3 the reference pulse $rrc(t)$ with a pulse duration of 2 ns is depicted. The leftmost part shows an example of a standard compliant UWB-pulse $p(t)$ and the right plot illustrates the normalized cross correlation $\Phi(\tau)$ between the pulse and the reference pulse. It can clearly be seen that the peak is above 0.8 for at least 0.5 ns and no sidelobe is greater than 0.3.

The whole UWB-PHY is built upon the fundamental frequency of 499.2 MHz, the peak pulse repetition frequency (PRF). Any center frequency is a multiple of that frequency. The reciprocal value of the peak PRF is called the chip duration T_chip and is approximately 2.0032 ns. This means that no two pulses can occur closer spaced than T_chip and the distance between any two pulses are multiples of that time.
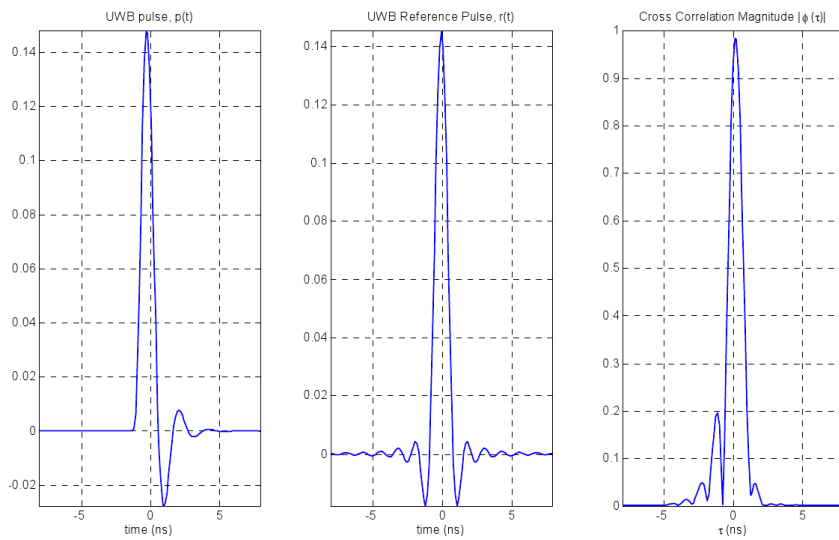
Figure 2.3: $p(t)$, $rrc(t)$ and $\Phi(\tau)$ [IEE07b] (©IEEE 2007)

Chapter 3

Impulse Response

One of the main tasks of the thesis was to use a previous built UWB-demonstrator [Buc08],[Gig10], take measurements with this demonstrator and extract the channel impulse responses (CIR) for ranging and positioning purposes. In previous works [Gig10], [Buc08], [Gei09], [Til10] the demonstrator was used for ranging purposes, although with different approaches. While [Buc08], [Gei09], [Til10] focus on the energy detector as receiver structure, [Gig10] uses both a coherent and a non-coherent receiver structure. In this work a coherent approach is presented.

The chapter is organized in the following way: First the demonstrator is presented in Section 3.1. Next the Receiver structure is presented in Section 3.2. At the end some considerations for different input signals (noise: Section 3.3 and an offset added to the input signal: Section 3.4) are discussed.

3.1 Transmitter

3.1.1 Demonstrator

The modular concept of the demonstrator (upper part) as well as the measurement setup for one Base station (lower part) can be seen in Figure 3.1.

As mentioned earlier, the demonstrator has been developed during previous works at the TU Graz in cooperation with TU Vienna and CISC Semiconductors. The main part of the demonstrator system is a Field Programmable Gate Array (FPGA) which produces the baseband pulses according to [IEE07b]. The FPGA is set to the desired peak PRF by
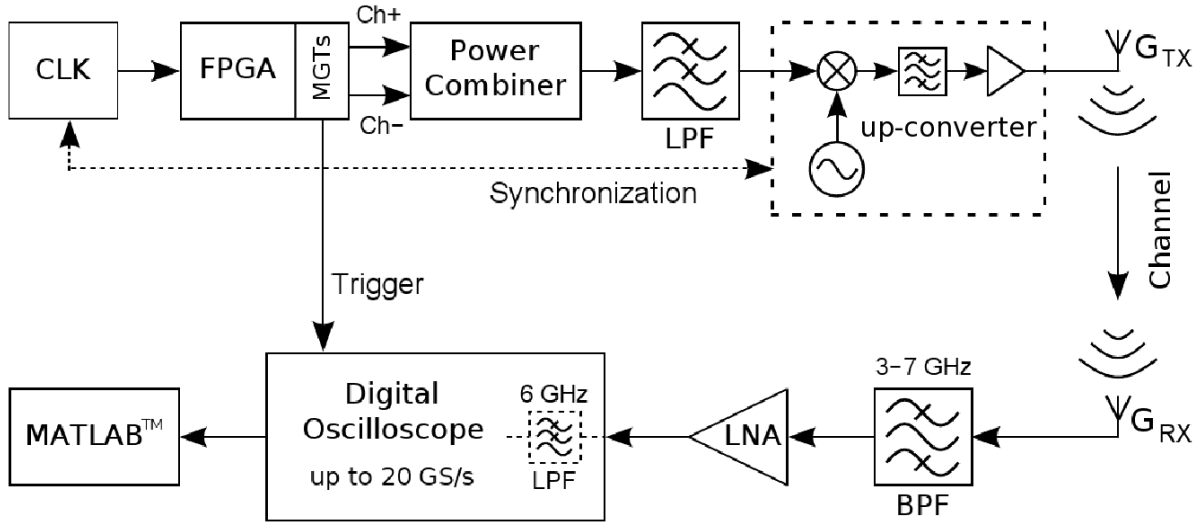
Figure 3.1: Modular concept of the demonstrator [GBA$^+$09] (©IEEE 2009)

a clock with 124.8 MHz. Two of the Multi-Gigabit Transceivers (MGT), which are high-speed serial Input/Outputs, are used to implement the positive (Ch+) and negative (Ch-) pulse sequences of the ternary data (cmp. Section 2.2). These sequences are combined by a passive power combiner. As the pulse shape has to fulfil constraints to be standard-compliant (cmp. Section 2.3) additional pulse shaping is done with the low-pass filter (LPF). This baseband signal is then modulated on the desired center frequency with a mixer, which is locked to the center frequency by the clock.[1] A bandpass filter (BPF) reduces the out-of band components of the mixer. At last a power amplifier amplifies the signal which is transmitted via the transmitter antenna to the receiver. One extra MGT is used to produce a trigger for the oscilloscope to start whenever a UWB-frame is sent. For further information on the demonstrator the reader is refered to [Buc08], [Gig10] or [GBA$^+$09].

In all the before-mentioned works, the demonstrator was used with a different center frequency of $f_c = 4492.8$ MHz whereas in this work the center frequency is $f_c = 3993.6$ MHz. In Table 3.1 the parameters of the IEEE 802.15.4a standard which were used in the demonstrator can be seen. In the next part a mathematical model for the transmitted signal is presented.

---

[1]Remember that the center frequency is a multiple of the peak PRF (described in Section 2.3)

Channel number	f_c in [MHz]	T_{chip} in [ns]	Code number	L	N_{sync}	N_{sfd}
2	3993.6	2.0032	6	16	64	8

Table 3.1: Used Parameters in the demonstrator

3.1.2 Transmitted Signal Model

In Section 2.2 a representation of one preamble symbol (Equation 2.1) was introduced, which will be used now to express the signal model for the preamble in a baseband or lowpass representation [Pro01]:

$$s_l(t) = \sqrt{E_p} \sum_{k=0}^{N_{sync}-1} \sum_{m=0}^{N_{code}-1} c_6[m]p(t - mLT_{chip} - kT_{1pr}) \qquad (3.1)$$

The first sum describes the repetitions of the preamble (N_{sync} times) while the second represents the N_{code} bits of the code. $c_6[m]$ are the code bits, the spreading factor is L, the pulse is expressed by $p(t)$, the chip duration is T_{chip} and T_{1pr} is the duration of one preamble symbol which is

$$T_{1pr} = LN_{code}T_{chip}.$$

The passband representation of the sent signal can easily be obtained by

$$s(t) = \text{Re}\big\{s_l(t)e^{j2\pi f_c t}\big\} = s_l(t)\cos(2\pi f_c t) \quad \text{since} \quad s_l(t) \in \mathbb{R}. \qquad (3.2)$$

In Figure 3.2 the beginning of this signal can be seen. One can clearly see the used preamble code $c_6 = [++00+00---+-0++-000+0+0-+0+0000]$. The difference of a $+1$ and a -1 can not be seen, as the signal is in the passband.

3.2 Receiver

The measurement setup for the receiver can be seen in Figure 3.1. The signal is received by an antenna and filtered by a BPF. This BPF shall reduce the out-of-band noise and attenuate interferer such as the Global System for Mobile Communication (GSM) and the 2.4 GHz ISM-band (Industrial, Scientific and Medical band) which is used in the Wireless-LAN (W-LAN) IEEE802.11b/g/n standards [IEE07a]. After filtering, the signal is amplified by a Low-Noise Amplifier (LNA) and fed into a Digital Sampling Oscilloscope
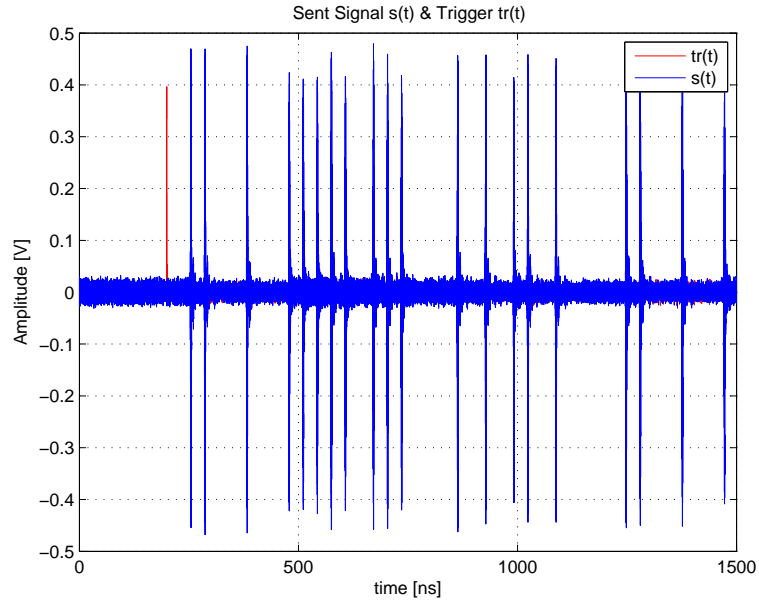
Figure 3.2: Sent Signal in Passband $s(t)$

(DSO) whose output is used for further signal processing.

3.2.1   Received Signal Model

The lowpass equivalent sent signal (Equation 3.1) is sent over the complex baseband channel

$$h_l(t) = h_c(t) + jh_s(t) \tag{3.3}$$

where $h_l(t)$ for simplicity also includes the effects of the receiver (RX) and the transmitter (TX) antenna as well as the BPF of the receiver shown in Figure 3.1. Moreover the channel is assumed to be constant for at least

$$T_{pr} = N_{sync}T_{1pr}$$

which is the duration of the SYNC part of the SHR (see Figure 2.1).

This leads to a received signal in baseband representation $r_l(t)$ which can easily be

found by convolving the sent signal $s_l(t)$ with the complex baseband channel.

$$
\begin{aligned}
r_l(t) &= \frac{1}{2} h_l(t) * s_l(t) \\
&= \frac{1}{2} \int_{-\infty}^{\infty} h_l(t-\tau) s_l(\tau) d\tau \\
&= \frac{1}{2} \sqrt{E_\mathrm{p}} \sum_{k=0}^{N_\mathrm{sync}-1} \sum_{m=0}^{N_\mathrm{code}-1} c_6[m] p(t - mLT_\mathrm{chip} - kT_\mathrm{1pr}) * h_\mathrm{c}(t) \\
&\quad + \frac{j}{2} \sqrt{E_\mathrm{p}} \sum_{k=0}^{N_\mathrm{sync}-1} \sum_{m=0}^{N_\mathrm{code}-1} c_6[m] p(t - mLT_\mathrm{chip} - kT_\mathrm{1pr}) * h_\mathrm{s}(t)
\end{aligned}
\tag{3.4}
$$

To get a shorter notation of Equation 3.4 we introduce two new functions

$$
a(t) = \frac{1}{2} \sqrt{E_\mathrm{p}} \sum_{k=0}^{N_\mathrm{sync}-1} \sum_{m=0}^{N_\mathrm{code}-1} c_6[m] p(t - mLT_\mathrm{chip} - kT_\mathrm{1pr}) * h_\mathrm{c}(t)
\tag{3.5}
$$

$$
b(t) = \frac{1}{2} \sqrt{E_\mathrm{p}} \sum_{k=0}^{N_\mathrm{sync}-1} \sum_{m=0}^{N_\mathrm{code}-1} c_6[m] p(t - mLT_\mathrm{chip} - kT_\mathrm{1pr}) * h_\mathrm{s}(t)
\tag{3.6}
$$

which leads to

$$
r_l(t) = a(t) + jb(t)
$$

To get the passband representation of $r_l(t)$, (3.4), (3.5) and (3.6) have to be combined to

$$
\begin{aligned}
r(t) &= \mathrm{Re}\{r_l e^{j2\pi f_c t}\} + \nu(t) \\
&= a(t) \cos(2\pi f_c t) - jb(t) \sin(2\pi f_c t) + \nu(t)
\end{aligned}
\tag{3.7}
$$

where $\nu(t)$ is additive white Gaussian noise. This signal is then fed into a Low-Noise Amplifier (LNA).

In the next section the way from analog to the discrete (sampled) signal is described.

3.2.2 Sampling

As we wanted to measure one whole UWB-frame, and the used Oscilloscope (an Agilent 54850 Infiniium) is able to acquire 1 Msamples, the highest usable sampling frequency is $f_\mathrm{s} = 2\,\mathrm{GHz}$, due to the fact that one UWB-frame is approximately $200\mu s$ long.
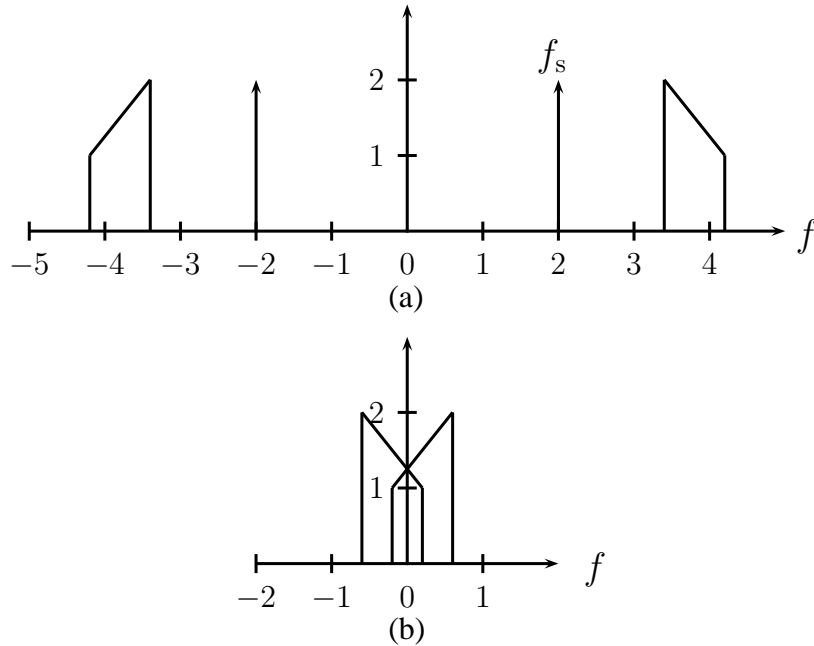
Figure 3.3: Aliasing: (a) shows the passband signal, (b) shows the baseband signal

The Nyquist-Shannon-Sampling theorem states that a bandlimited signal with a bandwidth of B is completely determined if sampled with $f_s \geq 2B$ [Sha98] which is fulfilled if the used sampling frequency is $\geq 998.4\,\mathrm{MHz}$. As the used sampling frequency is $f_s = 2\,\mathrm{GHz}$ the Nyquist-Shannon-Sampling theorem is not violated.

Due to the undersampling, shifted copies (mirror bands) of the analog spectrum develop. These mirror bands are according to [AVO99] shifted by integer multiples of the sampling frequency f_s. Therefore the absolute value of the center frequencies of the shifted bands are

$$|f_{c,\mathrm{low}}| = |f_c \pm i f_s| = 6.4, 1993.6, 2006.4, 3993.6, 4006.4, 5993.6, 6006.4, \cdots \qquad (3.8)$$

when the center frequency of the used channel is $f_c = 3993.6\,\mathrm{MHz}$ (see Table 3.1). As the bandwidth is $B = 499.2\,\mathrm{MHz}$ aliasing occurs which can be seen in Figure 3.3.

Normally it is not possible to recover the original signal if aliasing occurs [AVO99]. As we will see later in this chapter it is possible for this special problem due to the repetitions of the preamble.

By using Equation 3.7 the sampled signal can be described mathematically in the
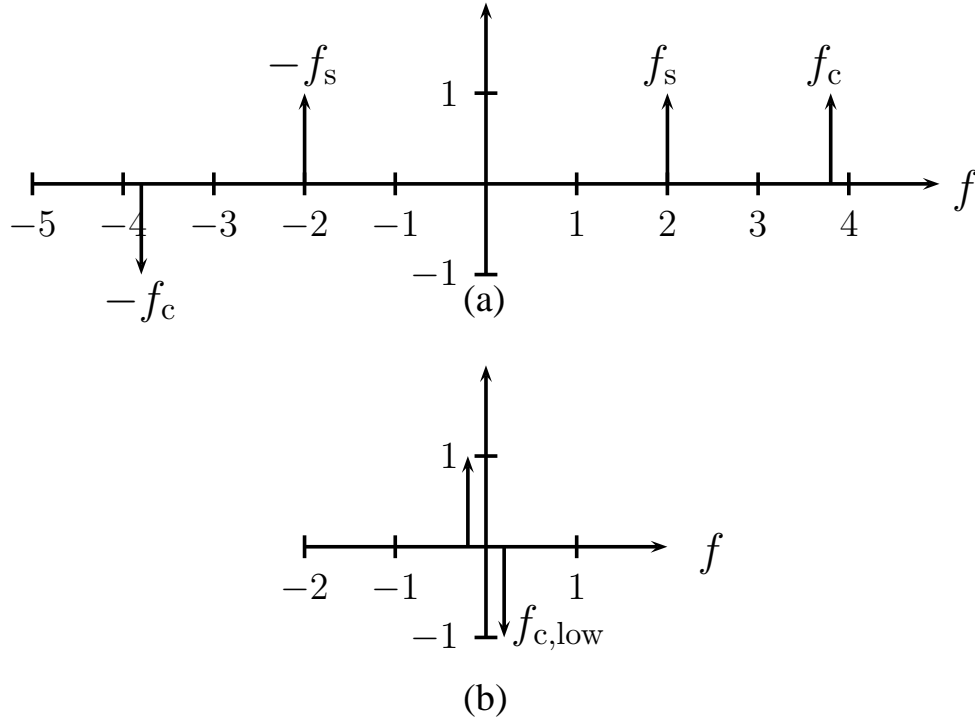
Figure 3.4: Frequency and Sign Change: (a) $\mathcal{F}\{\sin(2\pi f_c t)\}$, (b) mirror frequency $f_{c,low}$

following way

$$r(nT_s) = a(nT_s)\cos(2\pi f_{c,low} nT_s) \underbrace{+}_{!} b(nT_s)\sin(2\pi f_{c,low} nT_s) + \nu(nT_s) \qquad (3.9)$$

where $T_s = \frac{1}{f_s}$. The change of the sign can be explained by looking at Figure 3.4. The imaginary part of the Fourier transform of a sine is depicted in Figure 3.4a. If we now combine this with Equation 3.8 it is easy to get to Figure 3.4b. Here it is only shown for the smallest value of $|f_{c,low}|$. After comparing Figure 3.4 (a) and (b), the sign change in Equation 3.9 is obvious.

The signal in Equation 3.9 is the input to the coherent receiver, which is described in the next section.

3.2.3 Coherent Receiver

As described in the previous section, due to the used parameters, aliasing occurs. To be able to cope with that, the receiver structure in Figure 3.5 has been developed to estimate
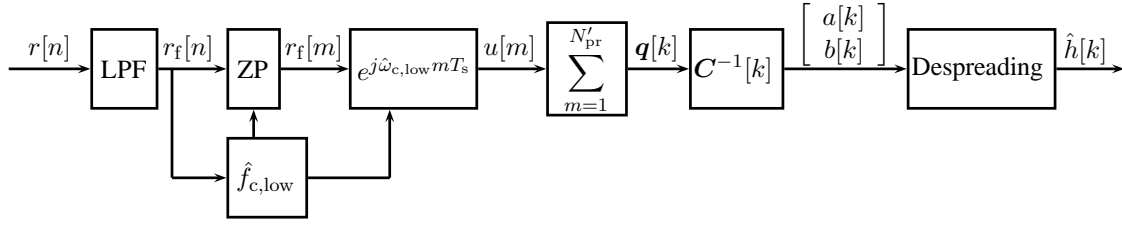
Figure 3.5: Coherent Receiver Structure

the channel impulse response. The incoming signal $r[n] = r(nT_\mathrm{s})$ is filtered with a low-pass filter to reduce out of band noise and attenuate interferer as W-LAN. The next step is to estimate the mirrored carrier frequency $\hat{f}_\mathrm{c,low}$ and change the sampling frequency to the estimated carrier frequency $\hat{f}_\mathrm{c}$ with zero-padding in frequency domain, to be able to use the repetitions of the preamble. Then the signal is shifted in the frequency domain by $\hat{f}_\mathrm{c,low}$ followed by summing up over the preambles and separating real and imaginary part. By multiplying with the inverse of the matrix $\boldsymbol{C}^{-1}[k]$ it is possible to reconstruct $a[k]$ and $b[k]$. Finally a despreading algorithm is applied to estimate the complex channel impulse response $\hat{h}[k]$.

In the next Sections, the individual steps of the solutions are explained.

Filtering

The received signal is according to Sections 3.2.1 and 3.2.2

$$r[n] = a[n]\cos(2\pi f_\mathrm{c,low} nT_\mathrm{s}) + b[n]\sin(2\pi f_\mathrm{c,low} nT_\mathrm{s})$$

The noise term $\nu[n]$ in Equation 3.9 is neglected for now, as it is described in Section 3.3.

This signal is filtered with the reference pulse $rrc(t)$, described in Section 2.3. In the upper subplot of Figure 3.6 the used UWB pulse $p(t)$, which was measured and is therefore superimposed by noise, and the reference pulse $rrc(t)$ can be seen. In the lower subplot, the magnitude response of the filter $rrc(t)$ can be seen. Frequencies above approximately 420 MHz are attenuated by 60 dB.

The main task of this LPF is to reduce the out-of-band noise to cope with interferers. W-LAN (IEEE 802.11.a/h/n(optional)) for example uses the ISM-band at 5 GHz [IEE07a] which is not filtered by the bandpass filter described in Section 3.2 (cmp Figure 3.1). Due to undersampling this band is mirrored to frequencies between 275 MHz and 850 MHz and
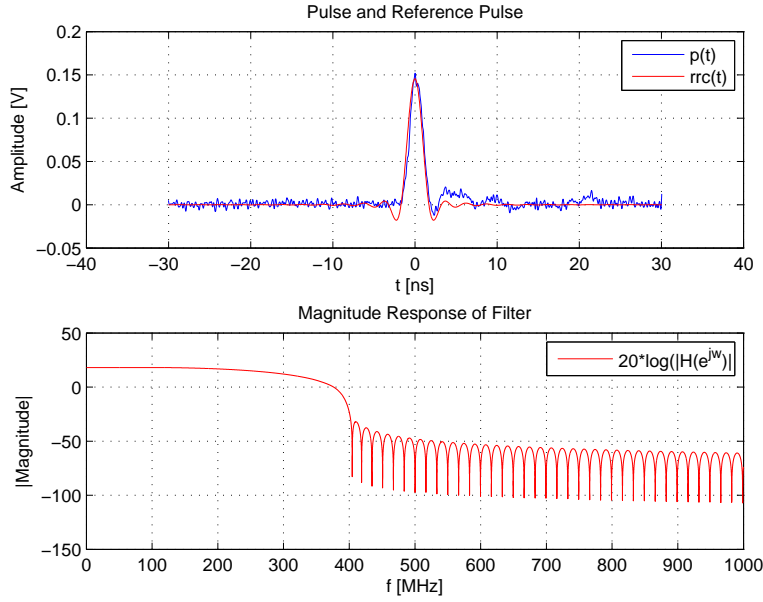
Figure 3.6: $p(t)$ (measured) and $rrc(t)$

it would influence the following signal processing steps heavily. This influence can be seen in Figure 5.2. By applying the LP filtering these frequency components are attenuated by up to 60 dB (see Figure 3.6).

The filtering process can be described mathematically in the time domain as the convolution

$$
\begin{aligned}
r_{\text{f}}[n] &= r[n] * rrc[n] \\
&= a_{\text{f}}[n] \cos(2\pi f_{\text{c,low}} n T_{\text{s}}) + b_{\text{f}}[n] \sin(2\pi f_{\text{c,low}} n T_{\text{s}})
\end{aligned}
\tag{3.10}
$$

where $rrc[n]$ is the energy-normalized reference pulse. The channel estimation would also work without the filtering, but it improves the results, especially if a W-LAN in the 5 GHz ISM-band is interfering.

Zero Padding and Frequency Estimation

To be able to use the repetitions of the preamble, the sampling frequency has to be changed to a multiple of the chip-frequency f_{chip}. This has been done with zero-padding in the frequency domain, which is an optimal $\frac{\sin(x)}{x}$ interpolation in the time domain
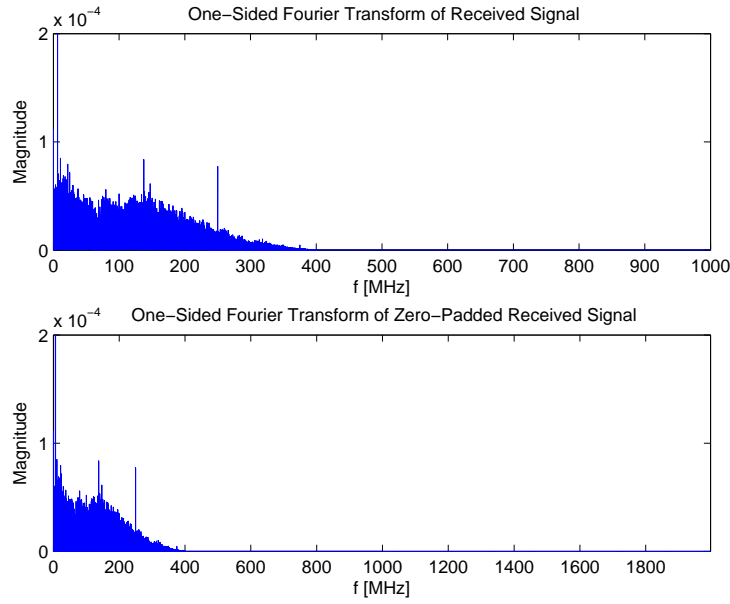
Figure 3.7: Zero Padding

and is illustrated in Figure 3.7. As with zero-padding it is only possible to increase the sampling frequency, it has been changed to $f'_s = 8f_{\text{chip}} = f_c$. According to [IEE07b] the carrier frequency tolerance is 20 ppm, hence it is important to have an exact estimate of it. Due to the undersampling only the mirrored carrier frequency $f_{c,\text{low}}$ can be estimated (cmp. Section 3.2.2). In [Kay88] it is stated, that the Power Spectral Density is the best solution if only one frequency in noise has to be estimated. This cannot be done directly by applying a Fourier transform and search for the maximum. Because the spacing of the frequency bins would be too large $(\frac{f_s}{N_{\text{samples}}} = 2000\,\text{Hz})$, only the first 10 MHz of the signal are taken into account, zero-padded in time domain and the power spectral density is calculated to estimate $\hat{f}_{c,\text{low}}$. With this technique it is possible to get a spacing of the frequency bins of 1 Hz in a reasonable processing time. The estimate for the carrier frequency is $\hat{f}_c = 2f_s - \hat{f}_{c,\text{low}}$ according to Section 3.2.2.

The interpolation changes the sampling frequency to f'_s and therefore also the number of samples to N'_{samples}. Therefore the signal is

$$r_f[m] = a_f[m]\cos(2\pi f_{c,\text{low}} m T'_s) + b_f[m]\sin(2\pi f_{c,\text{low}} m T'_s)$$

where $T'_\mathrm{s} = \frac{1}{f'_\mathrm{s}}$ is the new sampling time and $N'_\mathrm{samples} = N_\mathrm{samples}\frac{f'_\mathrm{s}}{f_\mathrm{s}}$ is the new number of samples.

Shifting

The spectrum of the signal now looks like Figure 3.8a. To get one of these spectra to the correct position of a baseband signal, it has to be shifted in the frequency domain by $\hat{f}_\mathrm{c,low}$,

$$
\begin{aligned}
u[m] &= r_\mathrm{f}[m]e^{(j2\pi \hat{f}_\mathrm{c,low}mT'_\mathrm{s})+j\alpha} \\
&= \frac{1}{2}a_\mathrm{f}[m](1 + e^{j(2\pi(\hat{f}_\mathrm{c,low}+f_\mathrm{c,low})mT'_\mathrm{s})}) + \frac{j}{2}b_\mathrm{f}[m](1 - e^{(j2\pi(\hat{f}_\mathrm{c,low}+f_\mathrm{c,low})mT'_\mathrm{s})}) \\
&= \frac{1}{2}a_\mathrm{f}[m](1 + e^{j(4\pi \hat{f}_\mathrm{c,low}mT'_\mathrm{s})}) + \frac{j}{2}b_\mathrm{f}[m](1 - e^{j(4\pi \hat{f}_\mathrm{c,low}mT'_\mathrm{s})}) \quad \text{if } \hat{f}_\mathrm{c,low} = f_\mathrm{c,low}
\end{aligned}
\tag{3.11}
$$

where the term $e^{j\alpha}$ is due to the fact, that the two signals are not phase synchronized. This term leads to a phase shift of the impulse response. By using Equation 3.11, the spectrum of the signal now looks like Figure 3.8b.

Equation 3.11 holds only if $\hat{f}_\mathrm{c,low} = f_\mathrm{c,low}$. An error in the frequency estimation leads to the result depicted in Figure 3.9, which has been made with an optimal input signal (the carrier frequency is exactly known) in a simulation environment. The x-axis shows the frequency error $\Delta f = f_\mathrm{c,low} - \hat{f}_\mathrm{c,low}$, while the y-axis shows the maximum of the amplitude of the estimated impulse response.

Repetitions of Preamble

In this step the sum over the preambles is calculated and the real and imaginary parts are separated.

$$
q[k] = \begin{bmatrix} \mathrm{Re}\left\{ \sum_{i=1}^{N_\mathrm{sync-1}} u[k + iN'_\mathrm{1pr}] \right\} \\ \mathrm{Im}\left\{ \sum_{i=1}^{N_\mathrm{sync-1}} u[k + iN'_\mathrm{1pr}] \right\} \end{bmatrix}
\tag{3.12}
$$

where $k \in [1, N'_\mathrm{1pr}]$ as opposed to $m \in [1, N'_\mathrm{pr}]$. Furthermore the sum is only computed over $N_\mathrm{sync-1}$ preambles because the first preamble symbol is not exactly the same as the other 63, due to the fact, that there was no preamble symbol sent in front of the first one.
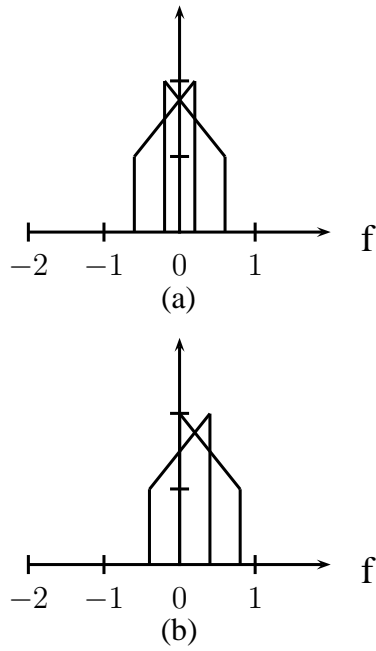
Figure 3.8: Shifting by $\hat{f}_{\text{c,low}}$ in the frequency domain
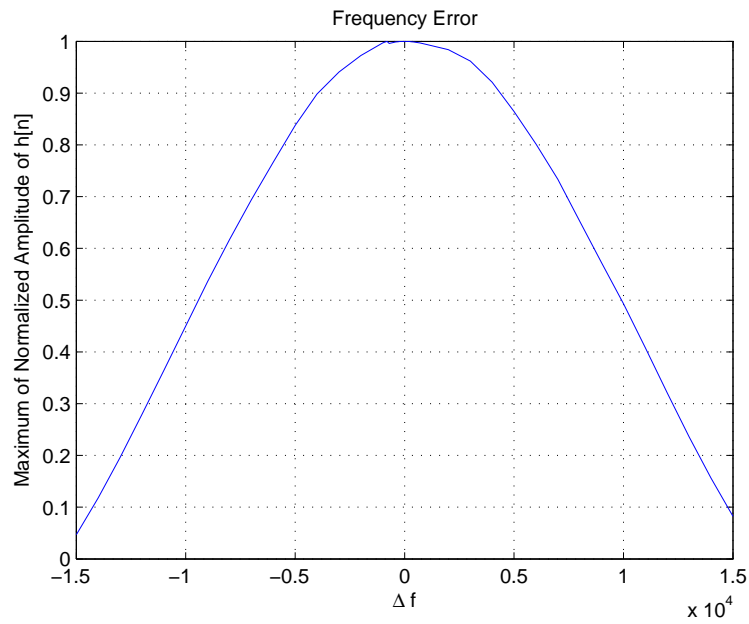
Figure 3.9: Error if $\hat{f}_{\text{c,low}} \neq f_{\text{c,low}}$

Matrix Multiplication with $C^{-1}[k]$

Equation 3.11 and Equation 3.12 can be combined to

$$
\begin{aligned}
q[k] &= \frac{1}{2}e^{j\alpha}
\begin{bmatrix}
\displaystyle\sum_{i=1}^{N_{\text{sync}}-1} 1 + \cos(4\pi\hat{f}_{\text{c,low}}[k + iN'_{\text{1pr}}]) & \displaystyle\sum_{i=1}^{N_{\text{sync}}-1} \sin(4\pi\hat{f}_{\text{c,low}}[k + iN'_{\text{1pr}}]) \\
\displaystyle\sum_{i=1}^{N_{\text{sync}}-1} \sin(4\pi\hat{f}_{\text{c,low}}[k + iN'_{\text{1pr}}]) & \displaystyle\sum_{i=1}^{N_{\text{sync}}-1} 1 - \cos(4\pi\hat{f}_{\text{c,low}}[k + iN'_{\text{1pr}}])
\end{bmatrix}
\begin{bmatrix}
a_{\text{f}}[k] \\
b_{\text{f}}[k]
\end{bmatrix} \\
&= \frac{1}{2}e^{j\alpha}C[k]
\begin{bmatrix}
a_{\text{f}}[k] \\
b_{\text{f}}[k]
\end{bmatrix}
\end{aligned}
\tag{3.13}
$$

Now it is easy to see how $a_{\text{f}}[k]$ and $b_{\text{f}}[k]$ can be calculated:

$$
\begin{bmatrix}
a_{\text{f}}[k] \\
b_{\text{f}}[k]
\end{bmatrix} e^{j\alpha} = 2C^{-1}[k]q[k]
\tag{3.14}
$$

It can clearly be seen from Equation 3.13 that the matrix $C[k]$ is approximately diagonal, as the summation over the cos and sin more-or-less cancel out. Now we also see, why the summation over the repetitions of the preamble is vital for the solution. By looking at matrix $C[k]$ and getting rid of the summation, it would get singular.

Despreading

Despreading has been done in a similar fashion as in [Gig10]. The difference is that for this problem circular despreading has to be used, as only one preamble symbol is available for despreading. This can be done by defining a matrix D which has the size $N'_{\text{1pr}} \times N_{\text{code}}$. This matrix has elements

$$
D_{k,p} = (a_{\text{f}}[\{(k-1)+(p-1)N'_{\text{c}}\} \mod N'_{\text{1pr}}+1] + jb_{\text{f}}[\{(k-1)+(p-1)N'_{\text{c}}\} \mod N'_{\text{1pr}}+1])e^{j\alpha}
\tag{3.15}
$$

where $k \in [1, N'_{\text{1pr}}]$ & $p \in [1, N_{\text{code}}]$ and

$$
N'_{\text{c}} = LT_{\text{chip}}f'_{\text{s}}
\tag{3.16}
$$

is the number of samples for one spreaded preamble bit. Interpulse-Interference (IPI) can occur ($N'_{1\text{pr}}$ can be greater than N'_{c}), due to the perfect circular autocorrelation properties of the code [Gig10]. In Figure 3.10 $\tilde{\boldsymbol{D}}^{\text{T}}$ is shown, which is $\boldsymbol{D}^{\text{T}}$ where the m-th row is multiplied with $c_6[m]$ and the zero-coded rows are cancelled [Gig10]. After approximately 10 ns the synchronized pulses can be seen. Every 32 ns code bits are sent. Therefore the next pulses occur at 42 ns and 74 ns. By summing over the rows of $\tilde{\boldsymbol{D}}^{\text{T}}$ respectively the columns of $\boldsymbol{D}$ multiplied with $\boldsymbol{c_6}$ the differently coded pulses cancel out and the impulse response can be calculated. This can be written as

$$\hat{\boldsymbol{h}} = 2\frac{\boldsymbol{Dc_6}}{M_1}e^{j\alpha} \tag{3.17}$$

where $M_1 = \frac{N_{\text{code}}+1}{2}$ because only the non-zero pulses are used for calculating the impulse response. The factor of 2 is due to Equations 3.5 and 3.6. As $e^{j\alpha}$ is only a phase shift and does not influence the absolute value of $\hat{\boldsymbol{h}}$, which is needed for ranging, it can be neglected. At approximately 20 ns a strong multipath component can be seen which also is seen in Figure 3.11 which shows the related impulse response which has been calculated by Equation 3.17. This estimated impulse response $\hat{\boldsymbol{h}}$ now includes the TX and the RX antenna, the analog BPF, the LNA, the digital LPF and the complex channel impulse response.

3.3 Noise Analysis

In this next part, the signal processing steps described by Figure 3.5 and the previous section are described, if the input signal is

$$r[n] = \nu[n]$$

where $\nu[n]$ is additive white Gaussian noise with

$$\nu[n] \ \ iid \ \ \mathcal{N}(0, \sigma^2) \tag{3.18}$$

where *iid* means independent, identically distributed which means, that

$$\text{E}\{\nu[n]\nu[n+m]\} = 0 \quad \text{for} \quad m \neq 0 \tag{3.19}$$
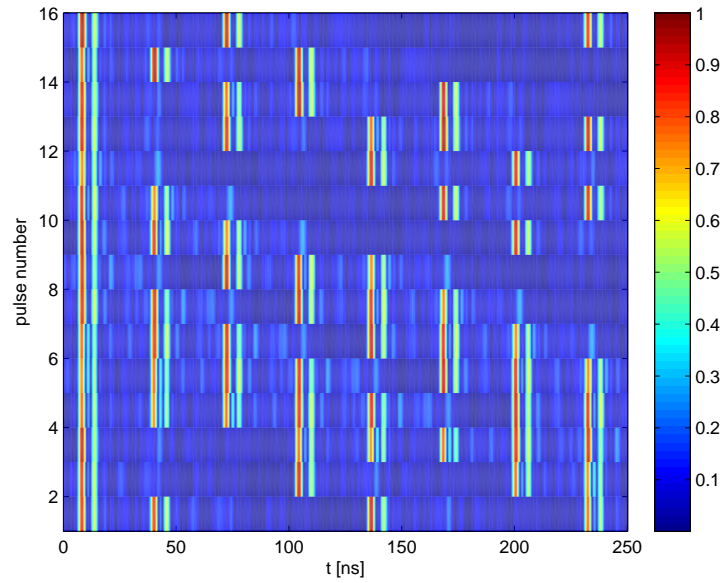
Figure 3.10: Despreading Matrix $\boldsymbol{D}^{\mathrm{T}}$
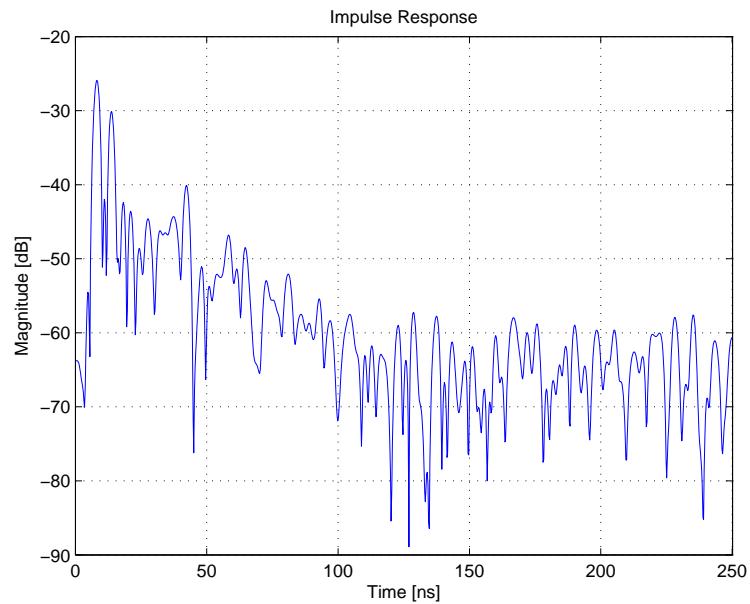
Figure 3.11: Impulse Response

Due to the summation over the repetitions of the preambles, it is necessary to use a random process description and not only a random variable description. The proofs for the distributions of the individual steps can be found in Appendix A.

Filtering

According to [Ham83] the distribution of the output of an FIR filter is

$$r_\mathrm{f}[n] \sim \mathcal{N}(0, \sigma^2 \sum_\mathrm{k} rrc^2[k]) \sim \mathcal{N}(0, \sigma^2)$$

if the input signal is white Gaussian with zero mean and variance σ^2. Since $\sum_\mathrm{k} rrc^2[k]$ is one (see Section 3.2.3), the distribution of the output is the same as the one for the input signal. However, this variable is now no longer *iid* . But it can be shown that

$$\mathrm{E}\{r_\mathrm{f}[n]r_\mathrm{f}[n+w]\} = 0 \quad \text{if } |w| \geq N_\mathrm{f} \tag{3.20}$$

where N_f is the order of the filter.

Zero Padding

Zero-Padding in the frequency domain does only add zeros to the Fourier transform of the signal (see Figure 3.7) and hence also only adds zeros to the power spectral density (PSD) of the signal. Due to the fact, that the variance is the integration of the PSD normalized by the sampling frequency, the variance of the signal is not changed by zero-padding.

$$r_\mathrm{f}[m] \sim \mathcal{N}(0, \sigma^2) \tag{3.21}$$

Shifting and Repetitions of Preamble

It is easier to look at these two steps together, because the random variables are no longer *iid* . As shown in Appendix A the distributions for the real- and imaginary-part

after shifting and summing up over the repetitions of the preamble are

$$
\boldsymbol{q}[k] \sim \begin{cases} \mathcal{N}\left(0, \sigma^2 \displaystyle\sum_{i=1}^{N_{\mathrm{sync}}-1} \cos^2(2\pi \hat{f}_{\mathrm{c,low}} T'_{\mathrm{s}}[k + iN'_{\mathrm{1pr}}])\right) \sim \mathcal{N}(0, \sigma^2_{\mathrm{sum},1}[k]) \\[4ex] \mathcal{N}\left(0, \sigma^2 \displaystyle\sum_{i=1}^{N_{\mathrm{sync}}-1} \sin^2(2\pi \hat{f}_{\mathrm{c,low}} T'_{\mathrm{s}}[k + iN'_{\mathrm{1pr}}])\right) \sim \mathcal{N}(0, \sigma^2_{\mathrm{sum},2}[k]) \end{cases}
$$

whose real and imaginary parts are again uncorrelated for $|w| \geq N_{\mathrm{f}}$, according to Equation 3.20. Moreover are the real- and imaginary part of $\boldsymbol{q}[k]$ now correlated

$$
\mathrm{E}\{\mathrm{Re}\{\boldsymbol{q}[k]\}\,\mathrm{Im}\{\boldsymbol{q}[k]\}\} =
$$

$$
= \sigma^2 \sum_{i=1}^{N_{\mathrm{sync}}-1} \cos(2\pi \hat{f}_{\mathrm{c,low}} T'_{\mathrm{s}}[k + iN'_{\mathrm{1pr}}]) \sin(2\pi \hat{f}_{\mathrm{c,low}} T'_{\mathrm{s}}[k + iN'_{\mathrm{1pr}}])
$$

$$
= \sigma^2_{\mathrm{cos,sin}}[k]
$$

Matrix Multiplication with $\boldsymbol{C}^{-1}[k]$

After multiplying with $\boldsymbol{C}^{-1}[k]$ $a_{\mathrm{f}}[k]$ and $b_{\mathrm{f}}[k]$ are obtained. Their distribution is

$$
a_{\mathrm{f}}[k] \sim \mathcal{N}(0, 4c_{11}^2[k]\sigma^2_{\mathrm{sum},1}[k] + 4c_{12}^2[k]\sigma^2_{\mathrm{sum},2}[k] + 8c_{11}[k]c_{12}[k]\sigma^2_{\mathrm{cos,sin}}[k])
$$
$$
\sim \mathcal{N}(0, \sigma^2_{\mathrm{C},1}[k])
$$

$$
b_{\mathrm{f}}[k] \sim \mathcal{N}(0, 4c_{21}^2[k]\sigma^2_{\mathrm{sum},1}[k] + 4c_{22}^2[k]\sigma^2_{\mathrm{sum},2}[k] + 8c_{21}[k]c_{22}[k]\sigma^2_{\mathrm{cos,sin}}[k])
$$
$$
\sim \mathcal{N}(0, \sigma^2_{\mathrm{C},2}[k])
$$

where $a_{\mathrm{f}}[k]$ and $b_{\mathrm{f}}[k]$ are again uncorrelated if $|w| \geq N_{\mathrm{f}}$ according to Equation 3.20. The variables $c_{11}[k]$, $c_{12}[k]$, $c_{21}[k]$, $c_{22}[k]$ are the entries of the inverse of matrix $\boldsymbol{C}[k]$ and are described in Equation 3.13.

Despreading

Despreading cannot only be described in a matrix notation, like Equation 3.17, but also in the following way

$$
\hat{h}[k] = \frac{2}{M_1} \sum_{i=1}^{N_{\mathrm{code}}-1} (a_{\mathrm{f}}[k + iN'_{\mathrm{c}}] + jb_{\mathrm{f}}[k + iN'_{\mathrm{c}}])c_6[i]
$$

Signal	Simulated Variance	Calculated Variance
$r[n]$	4.99	5.00
$r_{\mathrm{f}}[n]$	5.03	5.00
$\mathrm{Re}\{\boldsymbol{q}[k]\}$	161.73	157.47
$\mathrm{Im}\{\boldsymbol{q}[k]\}$	162.43	157.53
$a[k]$	0.163	0.159
$b[k]$	0.164	0.159
$\mathrm{Re}\left\{\hat{h}[k]\right\}$	0.0408	0.0397
$\mathrm{Im}\left\{\hat{h}[k]\right\}$	0.0409	0.0397

Table 3.2: Simulated and Calculated Variances for the different Signals

The mean of $\hat{h}[k]$ is

$$\mathrm{E}\left\{\hat{h}[k]\right\} = 0$$

since $a_{\mathrm{f}}[k]$ and $b_{\mathrm{f}}[k]$ are zero-mean.

The distribution for the real and imaginary part of $\hat{h}[k]$ are

$$\left[\begin{array}{c} \mathrm{Re}\left\{\hat{h}[k]\right\} \\ \mathrm{Im}\left\{\hat{h}[k]\right\} \end{array}\right] \sim \left[\begin{array}{c} \mathcal{N}(0, \frac{4}{M_1^2} \sum_{i=1}^{N_{\mathrm{code}}-1} \sigma_{\mathrm{C},1}^2[k + iN_{\mathrm{c}}']c_6^2[i]) \\ \mathcal{N}(0, \frac{4}{M_1^2} \sum_{i=1}^{N_{\mathrm{code}}-1} \sigma_{\mathrm{C},2}^2[k + iN_{\mathrm{c}}']c_6^2[i]) \end{array}\right] \sim \left[\begin{array}{c} \mathcal{N}(0, \sigma_{\mathrm{h}_1}^2[k]) \\ \mathcal{N}(0, \sigma_{\mathrm{h}_2}^2[k]) \end{array}\right]$$

In Appendix A it is shown that the maximum filter order N_{f} is

$$N_{\mathrm{f}} \leq N_{\mathrm{c}}' = LT\mathrm{chip}f_{\mathrm{s}}'. \tag{3.22}$$

In Figure 3.12 the variances of the real and imaginary part of $\hat{h}[k]$ are plotted. In contrast to the upper subplot, where the differences for different values of k cannot be seen, the lower subplot is done with zero suppression, hence a slight deviation is apparent. As this discrepancy is only about 0.5 %, it is said to be constant. Therefore the values in Table 3.2 show the mean values of the variances with respect to k, where the variance of the input signal has been chosen to be 5. The simulated and calculated values clearly match well. By looking at the variances of $\boldsymbol{q}[k]$ and $\hat{h}[k]$ the processing gain of 63 can be seen.

In Figure 3.13 the histograms of the previously described variables are depicted. As
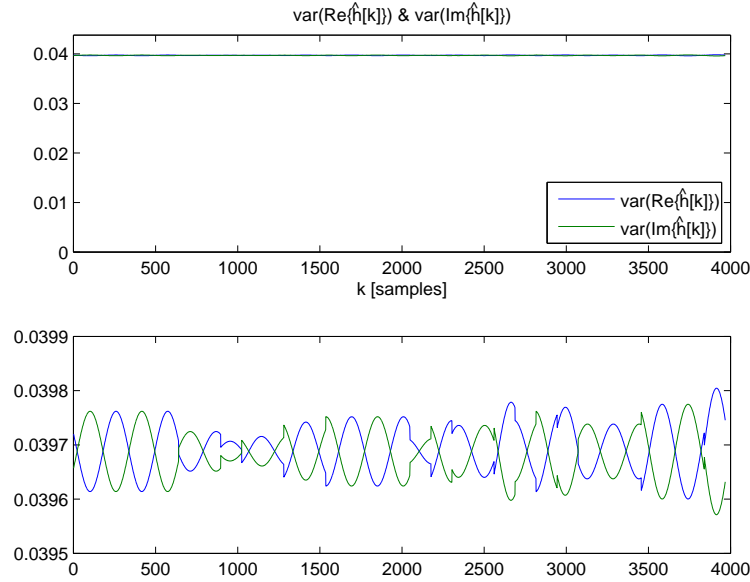
Figure 3.12: Variances of real and imaginary part of $\hat{h}[k]$

mentioned, filtering with $rrc(t)$ does not change the distribution of the input signal. Due to the shifting and adding of the preambles, the variances of $\boldsymbol{q}[k]$ get increased by the factor of $\sum_{i=1}^{N_{\mathrm{sync}}-1} \cos^2(2\pi \hat{f}_{\mathrm{c,low}} T'_{\mathrm{s}}[k + iN_{\mathrm{1pr}}])$, which is more or less a filtering operation and is depicted in the second row of the subplots. In the subplots in row three, the influence of the matrix multiplication with $\boldsymbol{C}^{-1}[k]$ is showed. In the last two subplots the final histograms for the real and imaginary part of $\hat{h}[k]$ are plotted.

3.4 Offset added to the Input Signal

In this part the influence of an offset added to the received signal is analysed. It is only done by means of a simulation. The input signal to the system is chosen to be

$$r[n] = 1$$

In Figure 3.14 the influence of the constant added to the input signal can be seen. Due to the signal processing steps, the offset added to the impulse response is not constant
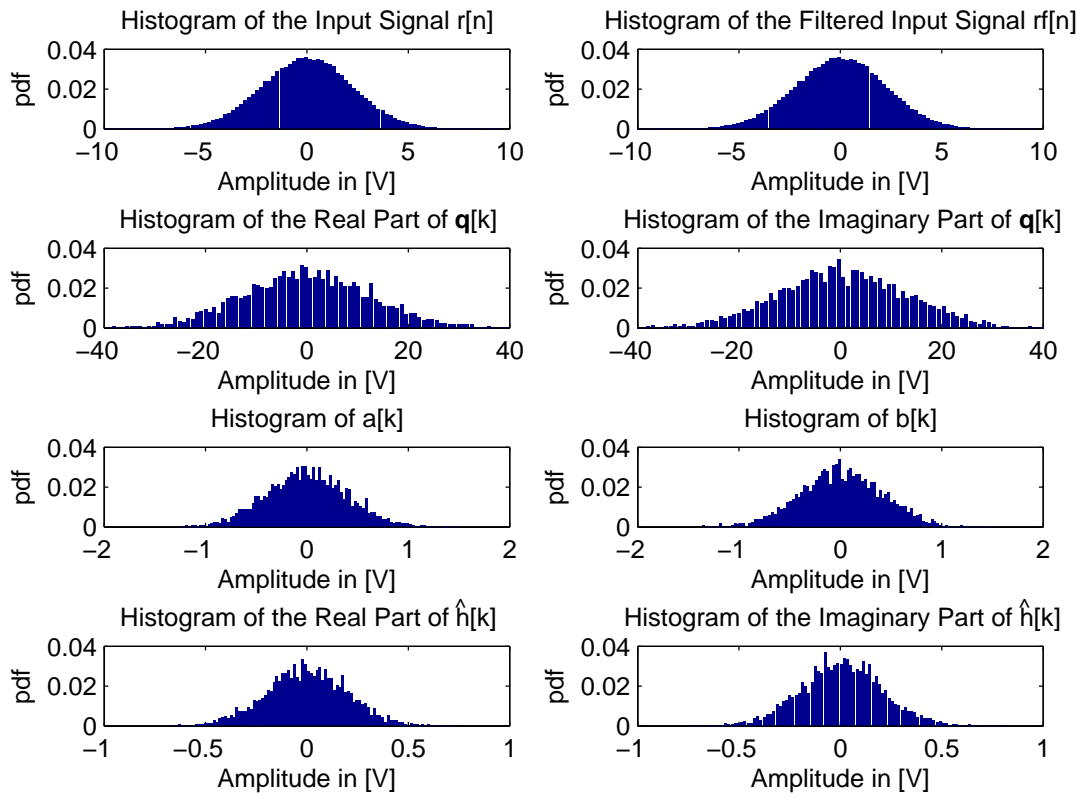
Figure 3.13: Histograms if $r[n] = \nu[n]$
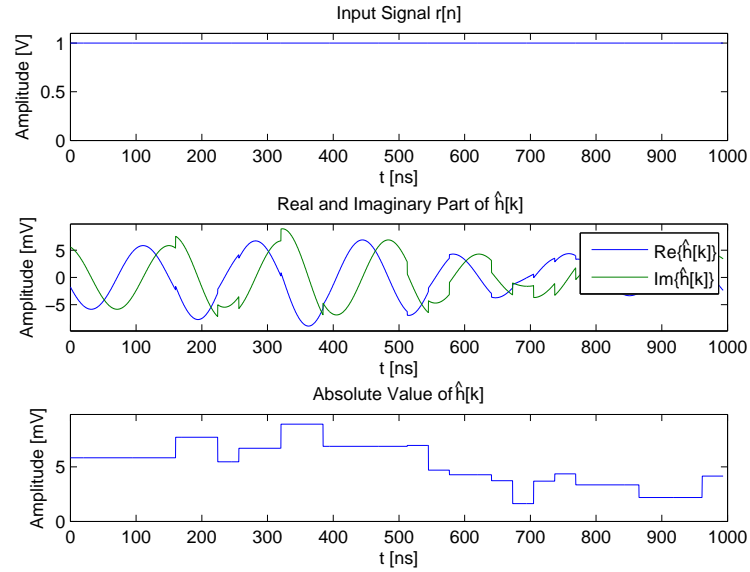
Figure 3.14: Received Signal $r[n] = 1$ and Impulse Response $\hat{h}[k]$

with respect to k. However, the constant is attenuated between $-57\,\text{dB}$ and $-41\,\text{dB}$.

This chapter has shown how a channel estimate can be calculated even though aliasing occurs during the sampling process. This is possible because the repetitions of the preamble are added coherently by using the signal processing steps explained in Section 3.2.3. Furthermore the processing gain and a bound for the filter order have been shown during the noise analysis.

The next chapter explains how the estimated impulse responses can be used to perform ranging and positioning.

Chapter 4

Ranging and Positioning

This chapter describes how ranging and positioning is performed. The impulse responses which were acquired with the receiver structure described in Chapter 3 are used to perform a leading edge detection as described in Section 4.1. These range estimates are utilized in Section 4.2 to position a tag in a room.

4.1 Ranging

It is the task of the ranging mechanism to detect the leading edge or the time of arrival (TOA) of the line of sight (LOS) component of the CIR. As this problem is vital for ranging, there is a wide field of literature.

The LOS-component of the CIR is not always the strongest multipath component (MPC) for example in a non-LOS (NLOS) scenario. Therefore the implemented approach is a threshold-based Jump-Back and Search-Forward (JBSF) algorithm, which is described for example in [ZS08]. In Figure 4.1 the JBSF mechanism can be seen. First of all the strongest MPC of the CIR is identified (green line). Next the algorithm jumps back a window length ω_{SB} (magenta line) and then searches forward for the first sample (red line) which exceeds a pre-defined threshold ζ. This leading-edge or LOS detection is estimated as

$$\hat{\tau}_{LOS} = \left\{ \min_k k \,\middle|\, ||\hat{h}[k]|| > \zeta \right\} T_s \tag{4.1}$$

where

$$\hat{h}[k] = \left[h[k_{max} - \frac{\omega_{SB}}{T_s}], \cdots, h[k_{max}] \right]$$
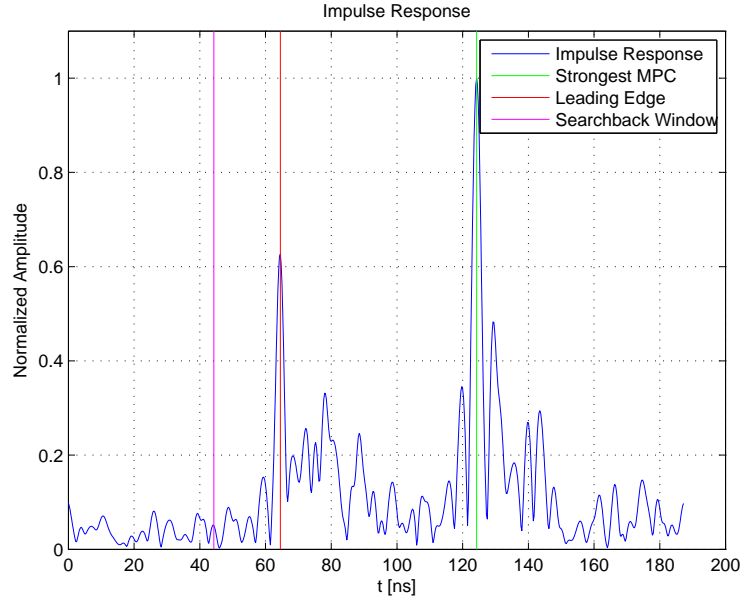
Figure 4.1: Jump-Back and Search-Forward algorithm

with k_{max} being the index of the strongest component.

Now the question arises how ω_{SB} has to be chosen. If the window length is too short it is possible that the leading edge arrives before the first sample taken into account. On the other hand, a too long window increases the possibility of a noise sample exceeding the threshold. In this work, the window length was chosen empirically with a value of 80 ns.

The next challenge is how to choose the threshold. This is a difficult task which is addressed for example in [DCF$^+$09]. If the threshold is chosen too large, the leading edge may not exceeds the threshold, while a too low one increases again the probability of a noise sample exceeding it. If for example in Figure 4.1 ζ is 0.7 the leading edge is not detected or on the other hand, if ζ is 0.1 a noise sample already exceeds the threshold. In [DW07] the threshold is defined to

$$\zeta = \overline{\nu}_{\hat{\mathrm{h}}} + c(|\hat{h}[k_{\mathrm{max}}]| - \overline{\nu}_{\hat{\mathrm{h}}}) \tag{4.2}$$

where $\overline{\nu}_{\hat{\mathrm{h}}}$ is the estimated mean amplitude of the noise in $|\hat{h}[k]|$ and $0 < c \leq 1$ is a user defined constant. In this work, ranging is performed with different values of c and the
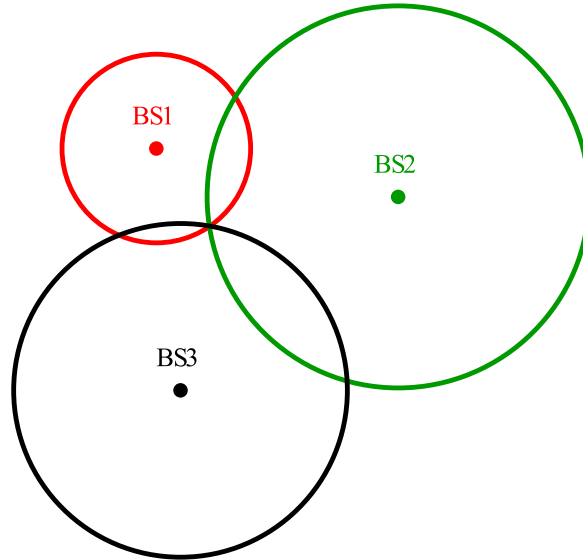
Figure 4.2: TOA Positioning with 3 BSs

best value with respect to the mean absolute error (MAE) is chosen.

The estimated distance can then be easily obtained from Equation 4.1 by multiplying with the speed of light

$$\hat{d} = \hat{\tau}_{\text{LOS}} v_{\text{c}} \tag{4.3}$$

where v_{c} is the speed of light.

If not only one range estimate, but three or more estimates to different BSs are available, positioning can be performed, which is explained in the next section.

4.2 Positioning

Based on range estimates to different base stations (BS) positioning can be performed. The possible position of the tag can be described by a circle around a BS. The availability of only two range estimates leads to a twofold solution because the circles of the two BS intersect in two points. By adding a third BS this ambiguity can be dismantled, hence three BSs are necessary for two-dimensional positioning, which can clearly be seen in Figure 4.2. For three-dimensional positioning a fourth BS would be required.

The range estimate to the i-th BS can be described as

$$\hat{d}_i = \sqrt{(x_i - x)^2 + (y_i - y)^2)}$$

where x_i and y_i are the coordinates of the i-th base station and x and y are the coordinates of the tag, which have to be estimated. This is done by solving a system of non-linear equations. This system consists of N_{BS}, the number of used BSs, equations

$$\hat{d}_1 = \sqrt{(x_1 - x)^2 + (y_1 - y)^2)}$$
$$\hat{d}_2 = \sqrt{(x_2 - x)^2 + (y_2 - y)^2)}$$
$$\hat{d}_3 = \sqrt{(x_3 - x)^2 + (y_3 - y)^2)}$$
$$\vdots$$
$$\hat{d}_{N_{\mathrm{BS}}} = \sqrt{(x_{N_{\mathrm{BS}}} - x)^2 + (y_{N_{\mathrm{BS}}} - y)^2)}$$

(4.4)

To solve this system, a linearisation is performed. This is done by Taylor series expansion and neglecting all the higher order components to obtain

$$\hat{d}_i = g_i(x, y) = g_i(x_0, y_0) + \left.\frac{\partial g_i}{\partial x}\right|_{x_0, y_0} (x - x_0) + \left.\frac{\partial g_i}{\partial y}\right|_{x_0, y_0} (y - y_0)$$

(4.5)

where (x_0, y_0) is the initial point for the algorithm and can be chosen randomly. $g_i(x_0, y_0)$ is the result of Equation 4.4 evaluated at x_0 and y_0. In the simulations the starting point is chosen as the mean of the BS coordinates. The partial derivatives are

$$\frac{\partial g_i}{\partial x} = \frac{x - x_i}{\sqrt{(x_i - x)^2 + (y_i - y)^2)}}$$
$$\frac{\partial g_i}{\partial y} = \frac{y - y_i}{\sqrt{(x_i - x)^2 + (y_i - y)^2)}}$$

(4.6)

and they are also evaluated at the initial point (x_0, y_0). Equation 4.5 can be transformed to

$$\hat{d}'_i = \hat{d}_i - g_i(x_0, y_0) + \left.\frac{\partial g_i}{\partial x}\right|_{x_0, y_0} x_0 + \left.\frac{\partial g_i}{\partial y}\right|_{x_0, y_0} y_0 = \left.\frac{\partial g_i}{\partial x}\right|_{x_0, y_0} x + \left.\frac{\partial g_i}{\partial y}\right|_{x_0, y_0} y$$

(4.7)

where all known terms are moved to the left side of the equation. By using a matrix notation for the coordinates, where $\boldsymbol{x} = \begin{bmatrix} x \\ y \end{bmatrix}$, and combining Equations 4.4 and 4.7 a

set of linear equations in matrix notation can be obtained

$$\hat{\boldsymbol{d}}' = \begin{bmatrix} \hat{d}'_1 \\ \vdots \\ \hat{d}'_{N_{\mathrm{BS}}} \end{bmatrix} = \boldsymbol{A}\hat{\boldsymbol{x}} = \begin{bmatrix} \left.\frac{\partial g_1}{\partial x}\right|_{x_0,y_0} & \left.\frac{\partial g_1}{\partial y}\right|_{x_0,y_0} \\ \vdots & \vdots \\ \left.\frac{\partial g_{N_{\mathrm{BS}}}}{\partial x}\right|_{x_0,y_0} & \left.\frac{\partial g_{N_{\mathrm{BS}}}}{\partial y}\right|_{x_0,y_0} \end{bmatrix} \begin{bmatrix} \hat{x} \\ \hat{y} \end{bmatrix} \tag{4.8}$$

where $\hat{\boldsymbol{x}}$ is an estimate for x and y, the coordinates of the mobile [1]. This set of linear equations can now be solved with a least squares (LS) approach:

$$\hat{\boldsymbol{x}} = (\boldsymbol{A}^{\mathrm{T}}\boldsymbol{A})^{-1}\boldsymbol{A}^{\mathrm{T}}\hat{\boldsymbol{d}}' \tag{4.9}$$

The LS approach has to be used to include more than two BSs in the solution. If the set of linear equations is solved for only two BSs, the solution would converge to one of the two intersections of the circles described in the beginning of this chapter, depending on the starting point. By adding the information of a third BS, the solution converges toward the correct position. Another aspect of the LS solution is that it is not bounded to three BSs but additional information from more BSs can easily be exploited.

As mentioned earlier, $\boldsymbol{x}$ is only an estimation, therefore the algorithm is an iterative one, where the estimated coordinates are the new starting point. This is repeated until the coordinates converge which can be expressed as

$$\boldsymbol{\epsilon} = \hat{\boldsymbol{d}}' - \boldsymbol{A}\hat{\boldsymbol{x}} \tag{4.10}$$

where $\boldsymbol{\epsilon}$ is the error vector for the coordinates. As a matter of fact, the algorithm does not always converge, because the range estimates are erroneous. It is also possible that the matrix $(\boldsymbol{A}^{\mathrm{T}}\boldsymbol{A})$ becomes singular, hence it can not be inverted. For these reasons, the algorithm has to be stopped after a finite number of iterations if the coordinates do not converge.

The next chapter shows how the previous two chapters can be combined to perform channel estimation, ranging and positioning with real measurement data. Furthermore parameters are estimated, which characterize the channel impulse response and can be used to compare different environments.

---

[1]Due to the linearisation an error occurs and therefore it is only an estimate

Chapter 5

Measurement Campaign

After obtaining a channel estimate $\hat{h}[k]$ in Chapter 3 and showing how a range and position estimate can be calculated in Chapter 4, measurements were performed in two different environments, a lecture hall and an office room. This is done to validate the solutions proposed in the previous two chapters. Another aspect is to analyse the ranging and positioning performance of the IEEE 802.15.4a standard as well as estimating system parameters like the pathloss exponent, the rms delay spread, the Ricean K-factor for the LOS component and the reverberation distance.

The next section outlines the measurement setup which was needed to implement the measurements. These have been performed in two different environments, a lecture hall called i2 and an office room called i10 hereafter. Section 5.2 presents the ranging and positioning results. In Section 5.3 the system parameters which were estimated are explained and results are shown for the two rooms.

5.1 Measurement Setup

In Figure 5.1 the measurement setup is depicted. The UWB-Demonstrator explained in Chapter 3.1.1 generates the transmit signal as well as a trigger which is used for synchronization. The transmit signal travels over the multipath channel to the three RX antennas. Before the signal is amplified by an LNA, a BPF reduces out of band noise and attenuates interference. It is worth mentioning, that the BPF for RX3 has a passband from 3.1 to 4.9 GHz while the other two BPFs have a passband from 3 to 7 GHz which means that RX3 is less influenced by interferer than the other two RXs. The LPF in
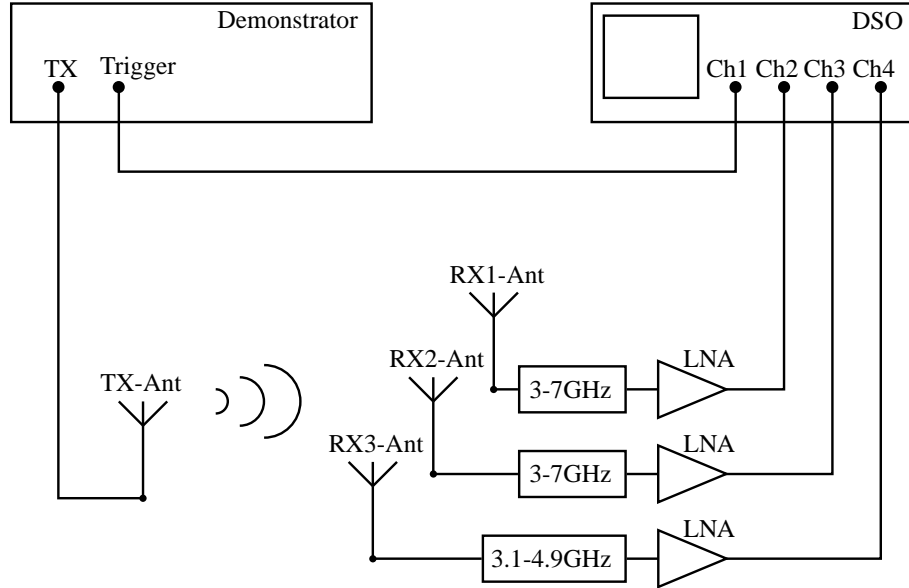
Figure 5.1: Measurement Setup

the coherent RX structure in Figure 3.5 improves the Signal-to-Interference Ratio also for RXs 1 and 2, but not as good as the analog filter, as the WLAN band gets mirrored to frequencies between 275 and 850 MHz, hence they interfere with the RX signal[1]. After amplification, the signals are fed into the DSO, where they are undersampled according to Section 3.2.2. In Figure 5.2 the influence of WLAN and the LPF in the RX is depicted. While in the left subplot the received signal is not LPF, the right subplot implements the LPF. It can clearly be seen that the LPF reduces the influence of WLAN by approximately 20dB.

In each room, the lecture hall i2 and the office room i10, 9 different positions have been measured. To measure not only the impulse response, but also obtain the power delay profile (pdp), which is found by taking the spatial average of $|h(\tau)|^2$ over a local area [Rap01]

$$\widehat{pdp}[k] = \frac{1}{N_{\text{grid}}} \sum_{i=1}^{N_{\text{grid}}} |\hat{h}_i[k]|^2 \tag{5.1}$$

where $\widehat{pdp}[k]$ is the power delay profile estimate and N_{grid} is the number of grid positions, it has been necessary to place the TX on a grid. This was a 5x3 grid with a spacing of 10 cm

---

[1]remember that the bandwidth of the received signal is 499.2 MHz

(a) without LPF

(b) with LPF
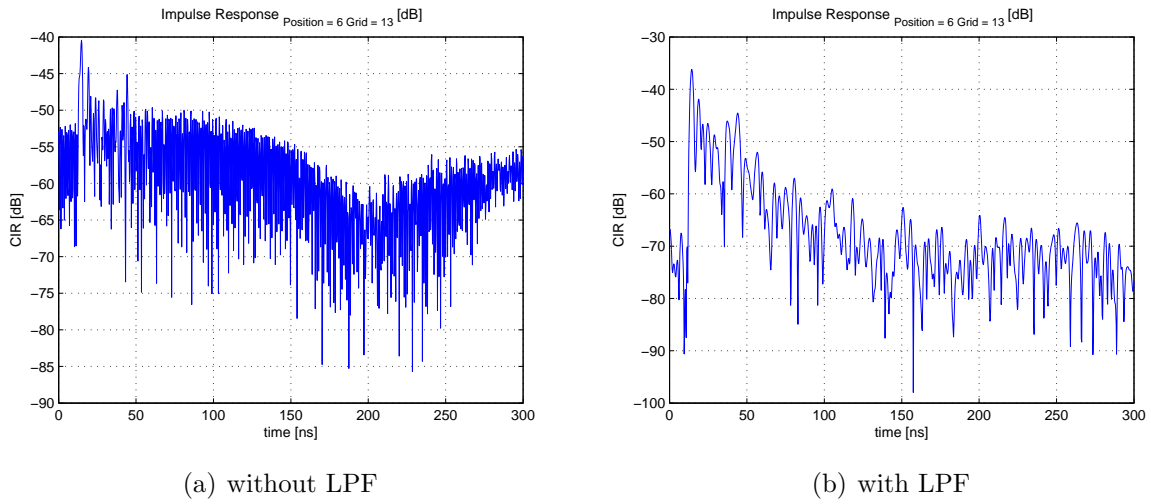
Figure 5.2: Influence of WLAN with and without LPF on $\hat{h}[k]$

Figure 5.3: Measurement Positions and Grid Description
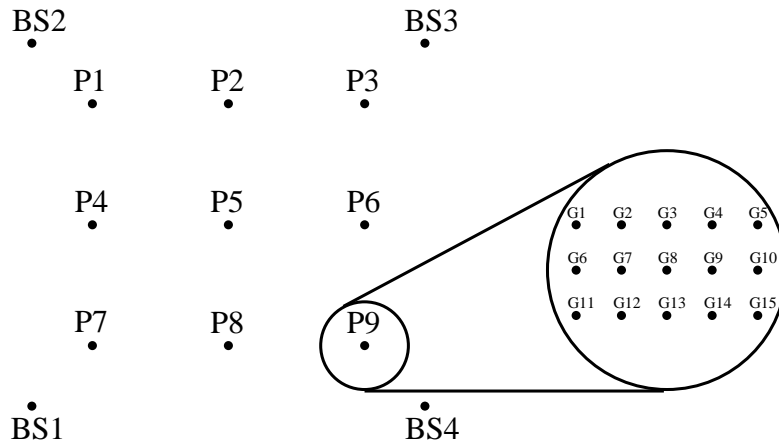
(a)   (b)
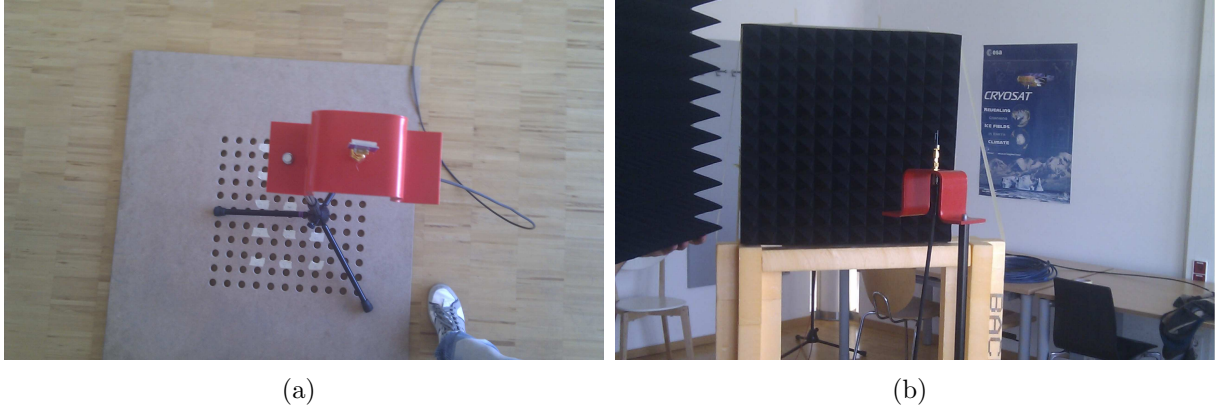
Figure 5.4: Grid and Absorber Material

	i2	LOS or NLOS	Passband of BPF in GHz	LNA	Antenna
BS1	(0,0)	LOS	3-7	Narda West	5-Cent
BS2	(0,8.5)	LOS	3-7	Miteq	Skycross
BS3	(7.57,8.5)	LOS	3.1-4.9	Miteq	5-Cent
BS4	(7.57,0)	LOS	3-7	Narda West	5-Cent
BS5	(0,8.5)	NLOS	3-7	Miteq	Skycross
BS6	(7.57,8.5)	NLOS	3.1-4.9	Miteq	5-Cent

Table 5.1: Coordinates (in [m]) and used measurement equipment of BSs in Room i2

(see Figure 5.4(a)) in each direction, which enables for a proper analysis of small-scale fading effects according to [IJN+06]. As we did not want to influence the measurement environment too much, the grid was made out of wood to get few additional reflections. This is graphically illustrated in Figure 5.3, where P1 to P9 are the measurement positions and G1 to G15 are the positions on the grid.

To measure not only LOS but also NLOS scenarios and get an additional BS, the rooms have been measured twice according to Figure 5.5 and 5.6. First, the BSs 1 through 3 were measured. In a second step the data for BSs 4 through 6 were obtained. In table 5.1 for room i2 and 5.2 for room i10 the positions of the BSs in the local coordinate system which is depicted in Figure 5.5 and 5.6 respectively, plus whether the LOS has been blocked or not, the used passband of the BPFs, the used LNA and the used Antenna can be seen[2]. The TX antenna was also the Skycross model. As both rooms are not really rectangular, it was difficult to position the BSs in the room. Therefore only one BS has

---

[2]a more detailed list of the measurement equipment can be found in Appendix B

	i10	LOS or NLOS	Passband of BPF in GHz	LNA	Antenna
BS1	(0,0)	LOS	3-7	Miteq	Skycross
BS2	(4.3,0)	LOS	3.1-4.9	Miteq	5-Cent
BS3	(0,-4.9)	LOS	3-7	Narda West	5-Cent
BS4	(4.3,-4.9)	LOS	3-7	Narda West	5-Cent
BS5	(0,0)	NLOS	3-7	Miteq	Skycross
BS6	(4.3,0)	NLOS	3.1-4.9	Miteq	5-Cent

Table 5.2: Coordinates (in [m]) and used measurement equipment of BSs in Room i10

Position Number	i2	i10
1	(0.555,7.270)	(1.080,-1.3500)
2	(3.785,7.270)	(2.160,-1.3500)
3	(7.015,7.270)	(3.240,-1.3500)
4	(0.555,5.470)	(1.080,-2.5500)
5	(3.785,5.470)	(2.160,-2.5500)
6	(7.015,5.470)	(3.240,-2.5500)
7	(0.555,1.370)	(1.080,-3.7500)
8	(3.785,1.370)	(2.160,-3.7500)
9	(7.015,1.370)	(3.240,-3.7500)

Table 5.3: Coordinates of the Measurement Positions (in [m]) in Room i2 and i10

been positioned with respect to the room and all the other BSs have been placed with respect to the first BS. In room i10, the texture of the parquet was used to place BS1 and BS2.

The lecture hall i2 is 15 m long, 12 m wide and 3.8 m high. The room has been optimized for acoustics a few years back, so the floor is carpeted, the walls and the ceiling are out of wood (absorber) and behind that is a concrete wall. As in most lecture halls, tables and benches out of wood with a metallic frame are built in as well as a metallic black board in the front of the room. In the back a chamber for technical purposes is situated, which has a window facing in direction of the black board.

The dimensions in office room i10 are 6 m times 7.5 m and it is 3.38 m high. The floor is a parquet and the ceiling is made out of concrete. Two of the walls are made also out of concrete, where one has a large window front, while the other two are gypsum plaster boards. In the room five tables, some chairs and two closets were present.

In Table 5.3 the coordinates of the measurement positions with respect to the local coordinate system can be seen. The stated coordinates are always the grid position 8,
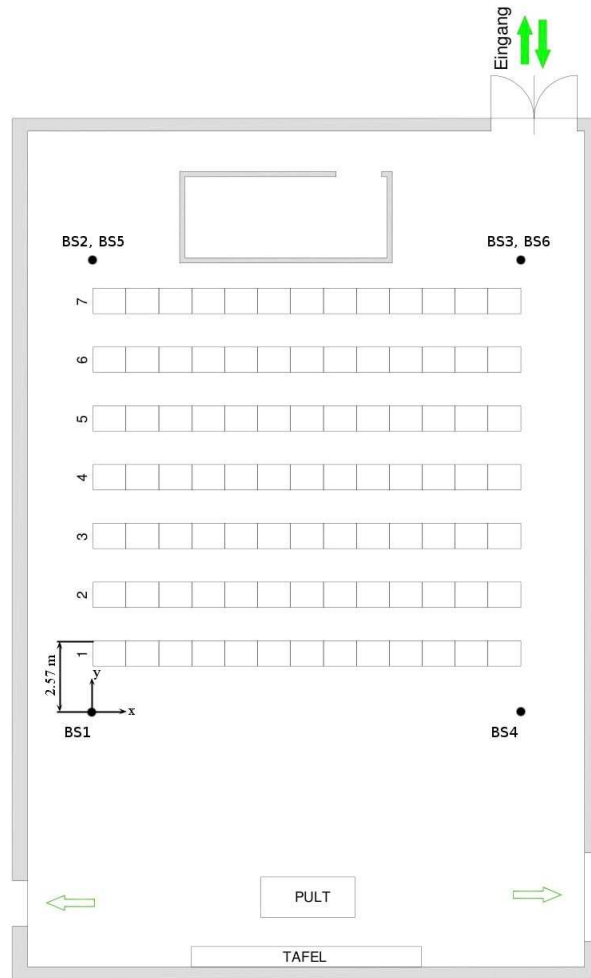
Figure 5.5: Placement of BS in Room i2
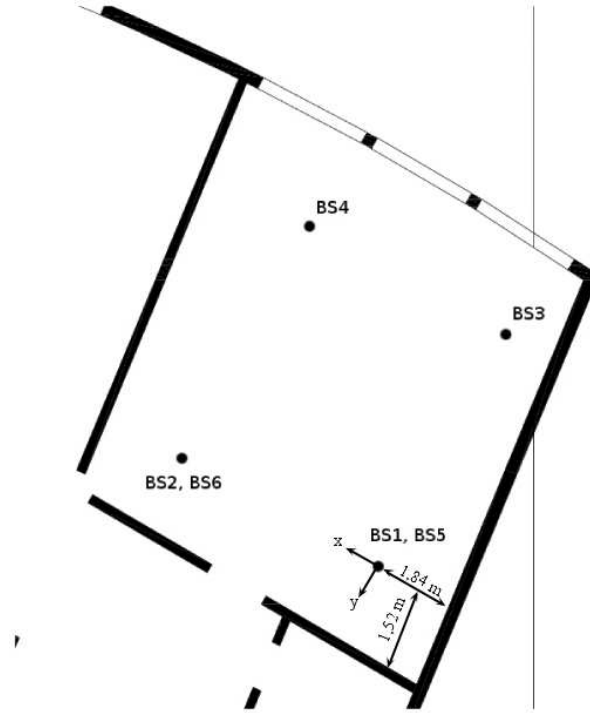
Figure 5.6: Placement of BS in Room i10

hence in the middle of the grid. Moreover was the antenna height of all BSs and the TX in room i2 1.8 m with respect to the lowest point in the lecture hall, and 1.67 m in room i10.

To get NLOS measurements, the direct path has been blocked by the pyramidal absorber EPP12, from Telemeter Electronic, which is seen in Figure 5.4(b). This pyramidal absorber has according to the manufacturer an attenuation in the used frequency range between $30 - 45$ dB.

Due to the fact, that the cables, the amplifiers and the filters have a delay, a calibration measurement for each BS had to be performed. The calibration distance has been set to 1 m. Because of this calibration and the fact that the first preamble is neglected for channel estimation according to Equation 3.12, the delays of the measurement equipment have not to be taken into account and do not influence the channel estimation.

	i2				i10			
	MAE	$\bar{e}_{\mathrm{rang}}$	$\sigma_{\mathrm{e_{rang}}}$	CEP_{90}	MAE	$\bar{e}_{\mathrm{rang}}$	$\sigma_{\mathrm{e_{rang}}}$	CEP_{90}
BS1	0.102	-0.001	0.130	0.218	0.102	0.096	0.055	0.155
BS2	0.081	0.018	0.100	0.170	0.109	-0.109	0.045	0.163
BS3	0.061	-0.007	0.078	0.130	0.159	-0.159	0.032	0.212
BS4	0.133	-0.012	0.164	0.253	0.108	0.101	0.071	0.184
BS5	0.246	0.170	0.488	0.873	0.213	0.184	0.361	0.314
BS6	0.185	0.127	0.376	0.404	0.223	-0.179	0.173	0.347

Table 5.4: Ranging Results: all values are in $[m]$

5.2   Ranging and Positioning Results

The theory of ranging and positioning was briefly described in Chapter 4 and is used now to calculate range and position estimates which have been obtained with the measurement setup explained in Section 5.1.

5.2.1   Ranging Results

To describe the performance of the range estimates the error e_{rang} is defined

$$e_{\mathrm{rang}} = \hat{d} - d \tag{5.2}$$

where $\hat{d}$ is the range estimate and d is the true distance between TX and RX.

In Table 5.4 the results for rooms i2 and i10 are listed where MAE is the mean absolute error, $\bar{e}_{\mathrm{rang}}$ is the mean of the error, $\sigma_{\mathrm{e_{rang}}}$ is the standard deviation of the error and CEP is the circular error probability (CEP) with respect to a specific percentage. The CEP_{90} means that 90 % of the range estimates show an error smaller than CEP_{90}. Normally the CEP is used for positioning, as it describes a circle for 2D and a sphere for 3D. Ranging can be viewed as 1D positioning, hence the CEP describes a line.

The maximum error for the four LOS BSs is 0.66 m in room i2 and 0.32 m in room i10. The maximum error for the two NLOS BSs is 3.59 m in room i2 and 1.95 m in room i10.

The two figures 5.7 and 5.8 show the ranging results graphically. The upper subplots depict the cumulative distribution function (cdf) of the absolute error. It can be seen that the range estimates for BS5 and BS6 are worse in comparison to the other BSs as these
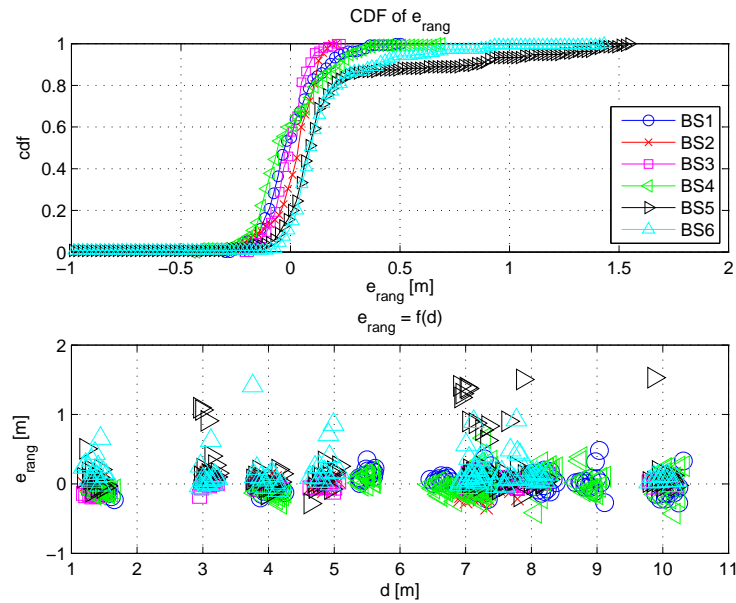
Figure 5.7: Ranging Results for i2

two are NLOS measurements. The range estimates for NLOS BSs are normally too large, as the electromagnetic wave bends around the obstacle (see Figure 5.4(b)) and therefore has to travel a larger distance.

Figure 5.7 conforms very well with the above mentioned statements. In Figure 5.8 however, all six BSs have an offset added to the ranging results. This is probably due to a misplacement of the BSs during the measurement, as the room was not rectangular, hence the placement of the BSs was difficult. The range estimates for BSs 1, 4 and 5 are always too large while BSs 2, 3 and 6 estimate the distance to the tag too short.

The lower subplots show the absolute error as a function of the distance between RX and TX. In these subplots, a main advantage of TOA-Ranging in combination with UWB can be seen, because the error does not increase if the distance increases. If the different MPCs of the CIR can be resolved, the error is not correlated with the distance.
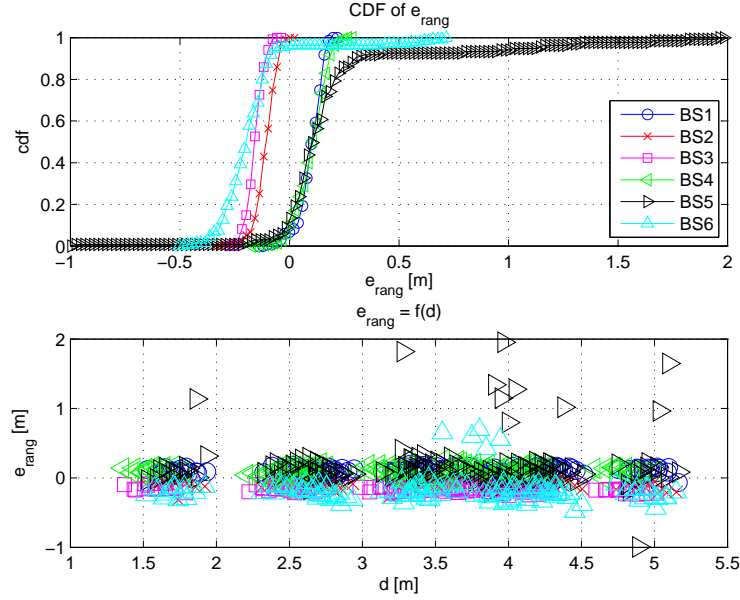
Figure 5.8: Ranging Results for i10

5.2.2   Positioning Results

For positioning the error is now two-dimensional, hence the errors in x-direction and in y-direction are defined as

$$e_{\mathrm{x}} = \hat{x} - x$$
$$e_{\mathrm{y}} = \hat{y} - y$$

where $\hat{x}$ and $\hat{y}$ are the estimated and x and y are the true coordinates of the tag. Further the absolute error for positioning is defined as

$$e_{\mathrm{pos}} = \sqrt{e_{\mathrm{x}}^2 + e_{\mathrm{y}}^2}.$$

Table 5.5 and 5.6 show the positioning results for room i2 and room i10, respectively. The first two columns indicate which BSs have been used to perform positioning[3] and how many of these had a blocked LOS. The next column states the CEP_{90}, while the

---

[3]the positions of the BSs in the rooms can be found in Figure 5.5 and 5.6 and in the Tables 5.1 and 5.2, respectively

BSs	$\#BS_{NLOS}$	CEP_{90}	MAE_{pos}	$\sigma_{e_{\text{pos}}}$	$\bar{e}_{\text{x}}$	$\sigma_{e_{\text{x}}}$	$\bar{e}_{\text{y}}$	$\sigma_{e_{\text{y}}}$
1 2 3	0	0.21	0.113	0.078	-0.004	0.089	-0.001	0.105
1 3 5	1	0.78	0.269	0.549	0.116	0.412	-0.100	0.425
1 2 3 4	0	0.23	0.123	0.078	0.004	0.100	-0.001	0.110
1 2 4 6	1	0.34	0.178	0.215	-0.047	0.237	-0.039	0.138
1 4 5 6	2	0.60	0.256	0.341	0.033	0.367	-0.084	0.198

Table 5.5: Positioning Results for Room i2: all values in $[m]$

last six columns present the MAE of the absolute positioning error, the corresponding standard deviation $\sigma_{e_{\text{pos}}}$, the mean of the positioning error in x- and y-direction as well as the associated standard deviations.

From Table 5.5 it can be seen, that the positioning works very well if only LOS BSs are used. Moreover is the performance with 3 BSs nearly the same as with 4 BSs for the LOS scenario. The benefit of the additional information of the fourth BS can be seen by looking at rows 2 and 4. Both scenarios have one NLOS BS, but the CEP_{90} is more or less half if a fourth BS is used. Even the results of row 5, where two NLOS BSs were used, are better. Moreover it can clearly be seen, that the positioning performance decreases with additional NLOS BSs.

In Figure 5.9 the estimated and true positions of the transmitter are plotted. The position estimates conform very well with the true positions.

This can even better be seen in Figure 5.10. In the left subplot the CDF of the absolute position error is plotted. The CDFs for row 1 and 3 in Table 5.5 are only slightly different, as both contain only LOS measurements. As described earlier, the additional information of a fourth BS leads to a performance increase. In the right subplot the error position with respect to the true position is depicted as well as the CEP_{90}[4]. By looking at the red markers (x) an interesting phenomenon can be explained. As the used NLOS BS (BS5) was positioned in the top left corner of the room and the range estimates are normally too large for an NLOS BS, the position estimates are pushed to the lower right corner of the room.

In Table 5.6 the results of Table 5.5 are conformed. The position estimates in room i10 are slightly better than in room i2.

In both rooms the position estimates show no significant deviation in x- and y-direction

---

[4]It is important to mention, that for better readability the limits for all the axes have been set to ± 2; thus some outliers are not included in the plot
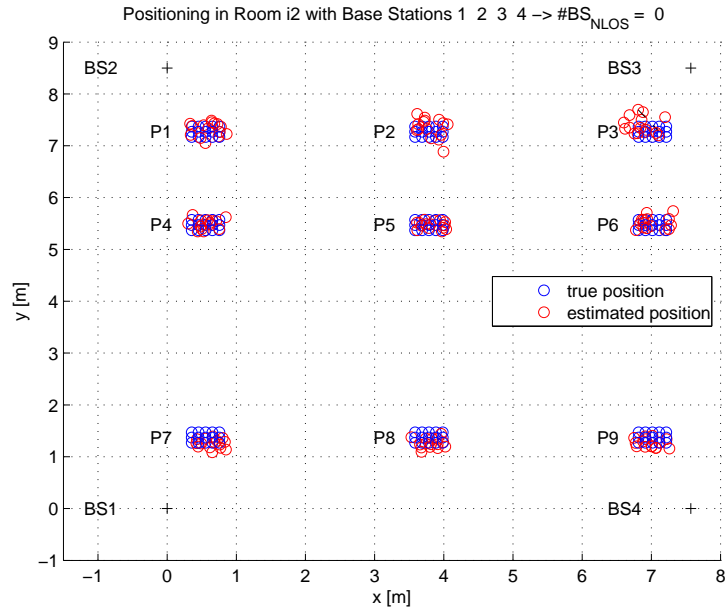
Figure 5.9: Positioning in Room i2 with 4 BSs with only LOS measurements
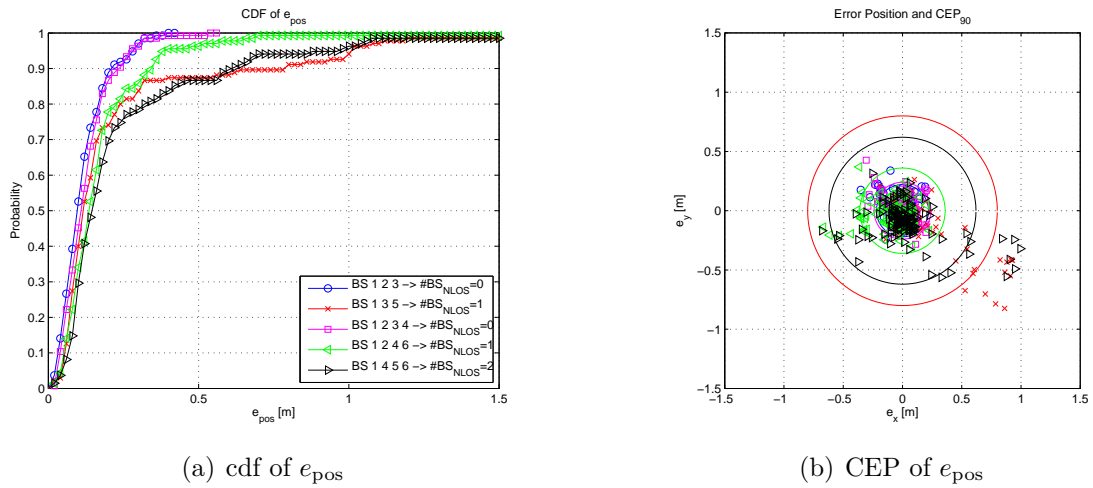

(a) cdf of e_{pos}

(b) CEP of e_{pos}

Figure 5.10: Positioning in room i2 for different scenarios

BSs	$\#BS_{NLOS}$	CEP_{90}	MAE_{pos}	$\sigma_{e_{\text{pos}}}$	$\bar{e_x}$	σ_{e_x}	$\bar{e_y}$	σ_{e_y}
1 2 3	0	0.18	0.112	0.089	0.045	0.078	-0.075	0.084
2 3 5	1	0.37	0.207	0.261	0.099	0.212	-0.124	0.200
1 2 3 4	0	0.09	0.051	0.032	-0.018	0.032	-0.009	0.045
2 3 4 5	1	0.14	0.100	0.161	0.019	0.145	-0.033	0.118
3 4 5 6	2	0.41	0.129	0.173	0.042	0.164	-0.010	0.134

Table 5.6: Positioning Results for Room i10: all values in $[m]$

(a) cdf of e_{pos}

(b) CEP of e_{pos}
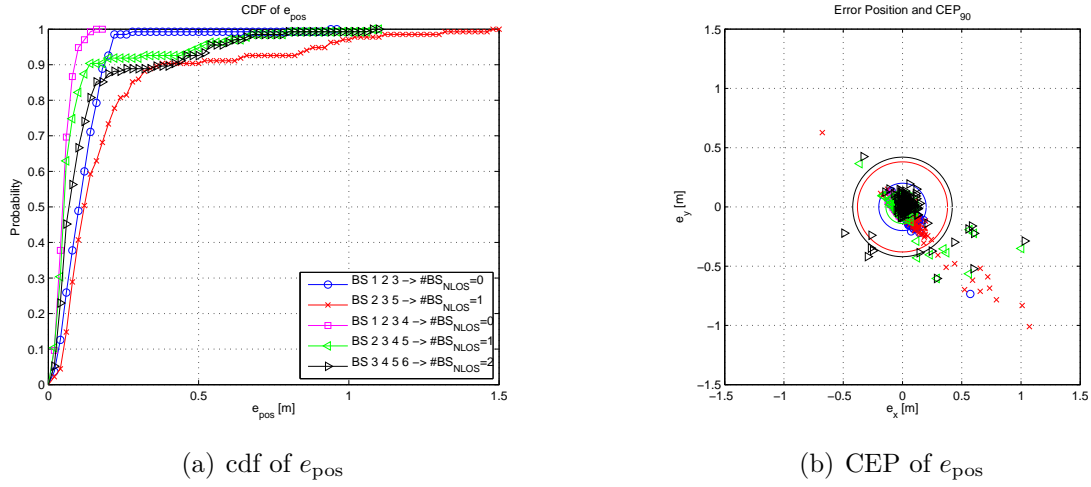
Figure 5.11: Positioning in Room i10 for different scenarios

which can be seen from $\bar{e_x}$ and $\bar{e_y}$ in both tables and the right subplots in Figure 5.10 and 5.11. In room i10 this result would not be expected, since the range estimates are superimposed by an offset (see column 7 in Table 5.4). The good positioning result stem from the fact that the sign of the offset of opposite BSs is the same. For example if BSs 1 through 4 are used for positioning, BSs 1 and 4 both push the position estimate to each other, hence the position algorithm converges toward a point in between these two wrong range estimates. The same holds true for BSs 2 and 3.

5.3   Estimated Channel Parameters

In this section, the channel parameters which have been estimated are presented. All these parameters depend on the position of the LOS component. To get correct parameters even if the LOS is not estimated correctly, the parameters have been calculated with the true

distance, hence they do not depend on the range estimate.

5.3.1   Pathloss Model

The pathloss PL in dB is defined as

$$PL = 10 \log \frac{P_{\text{TX}}}{P_{\text{RX}}} = 10 \log \frac{E_{\text{P}}}{T_{\text{s}} \sum_{n=0}^{N-1} |\hat{h}'[k]|^2} \tag{5.3}$$

according to [Gig10], where P_{TX} is the transmit power, P_{RX} is the received power and $\hat{h}'[k]$ is $\hat{h}[k]$ if $|\hat{h}[k]|$ is above the noise level while $\hat{h}'[k]$ is zero elsewhere. N corresponds to the maximum excess delay, which has been chosen to be $200\,\text{ns}$, and limits the estimated channel response to the most significant part. The pathloss model defined by [Rap01] is

$$PL(d) = PL(d_0) + 10\eta \log \frac{d}{d_0} + S \tag{5.4}$$

where $PL(d)$ is the pathloss at distance d, $PL(d_0)$ is the pathloss at the reference distance of $d_0 = 1\,\text{m}$, η is the pathloss exponent and S is a zero-mean log-normal shadowing random variable with a standard deviation of σ_{s}.

Table 5.7 shows the values of the pathloss models for the two measured rooms. Each BS has slightly different model parameters, due to the different positions in the room. BS5 and BS6, the two NLOS measurements, have both a very small pathloss exponent, because the LOS component is attenuated heavily, while the power in the other MPCs stays more or less the same, even for larger distances, which can also be seen in Section 5.3.4. The pathloss exponent is smaller than two[5] for all BSs, due to the reflections from the walls which keep the energy inside the room, hence more energy is coming to the receivers in comparison to free space.

In Figure 5.12 the measured and modelled pathlosses with respect to the distance can be seen.

---

[5]the pathloss exponent in free space is two, as the power of the received signal reduces with the square of the distance

	i2			i10		
	$PL(d_0)$	η	σ_s	$PL(d_0)$	η	σ_s
BS1	19.98	1.51	1.64	17.45	1.31	1.37
BS2	16.70	1.62	1.89	25.35	1.55	1.03
BS3	16.33	1.13	1.43	14.36	1.54	1.11
BS4	21.10	1.38	1.93	14.70	1.59	1.12
BS5	28.29	0.63	1.57	26.03	0.73	1.56
BS6	25.40	0.41	1.61	33.20	1.03	1.51

Table 5.7: Pathloss Model Parameters
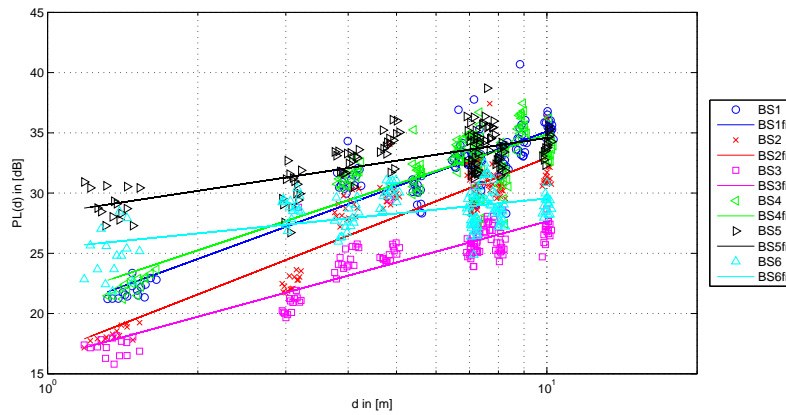
(a) i2
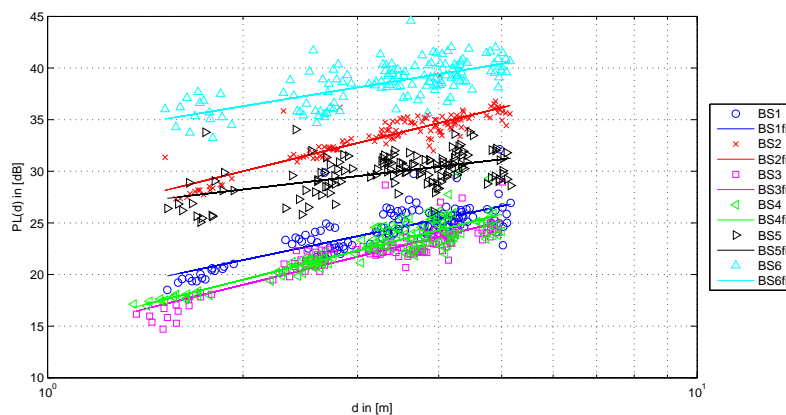
(b) i10

Figure 5.12: Pathloss of the measurement campaign

5.3.2   Mean Excess Delay and RMS Delay Spread

The mean excess delay $\bar{\tau}$ and the rms delay spread τ_{rms} are important parameters to compare different multipath channels as they vary for different environments. The mean excess delay is the first moment of the power delay profile and defined by [Rap01] to be

$$\bar{\tau} = \frac{\sum\limits_{k=0}^{N-1} \tau_k \widehat{pdp}'[k]}{\sum\limits_{k=0}^{N-1} \widehat{pdp}'[k]} \tag{5.5}$$

where $pdp'[k]$ is defined in a similar fashion as $\hat{h}'[k]$ and τ_k is the excess delay of the k-th sample. The rms delay spread is also defined by [Rap01] to

$$\tau_{\mathrm{rms}} = \sqrt{\overline{\tau^2} - \bar{\tau}^2} = \sqrt{\frac{\sum\limits_{k=0}^{N-1} \tau_k^2 \widehat{pdp}'[k]}{\sum\limits_{k=0}^{N-1} \widehat{pdp}'[k]} - \left(\frac{\sum\limits_{k=0}^{N-1} \tau_k \widehat{pdp}'[k]}{\sum\limits_{k=0}^{N-1} \widehat{pdp}'[k]}\right)^2} \tag{5.6}$$

and is the second centralized moment of the power delay profile.

In Figure 5.13 the cdf's of τ_{rms} for all BSs in both rooms are plotted. In room i2 the BSs 2, 3, 5 and 6 have longer rms delay spreads than BSs 1 and 4, because the window in the back of the room leads to a lot of strong MPCs that arrive significantly later than the LOS component. Therefore, the rms delay spread is longer for the BSs in the back of the room. In room i10 a similar result is visible. BSs 3 and 4 which are close to the window have a longer rms delay spread, than the other BSs.

In Figure 5.14 the mean excess delay is depicted which is highest for the NLOS BSs. While the rms delay spread shows no significant difference for the two measured rooms, the mean excess delay is higher for room i2.

5.3.3   Ricean K-factor

Another parameter which can be used to compare multipath channels is the Ricean K-factor for the LOS component. It is a measurement of the power in the LOS component
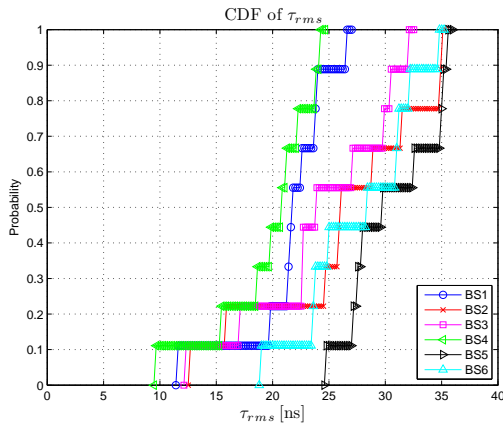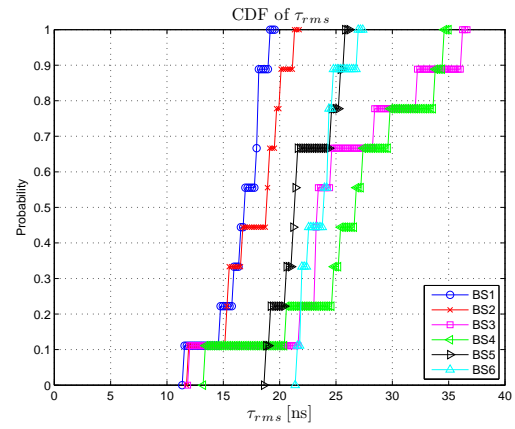
(a) i2   (b) i10

Figure 5.13: cdf of τ_{rms}
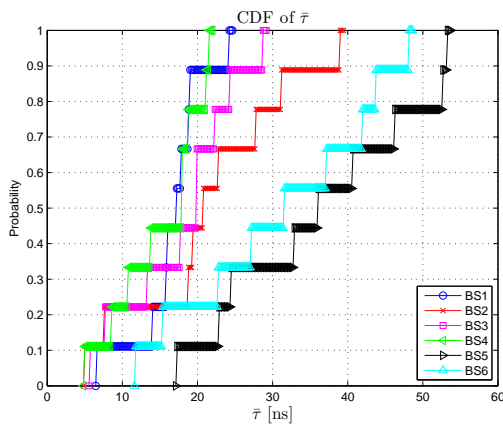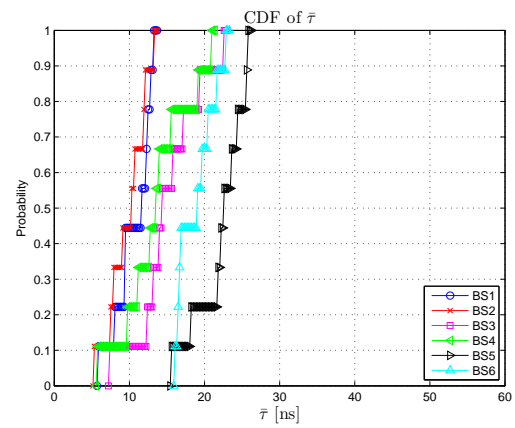
(a) i2   (b) i10

Figure 5.14: cdf of $\bar{\tau}$

(a) i2   (b) i10
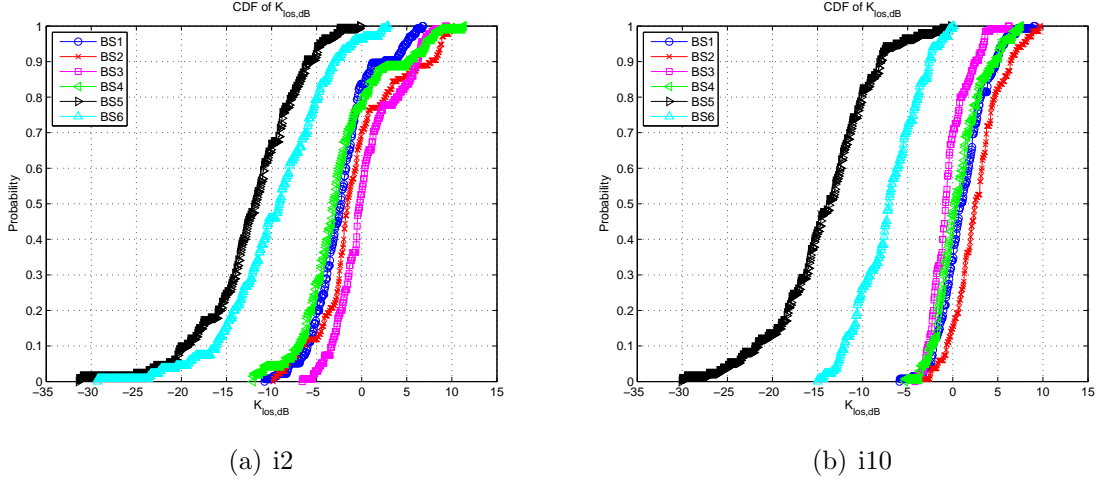
Figure 5.15: cdf of $K_{\mathrm{los,dB}}$

compared to the power in the scattered MPCs. It is defined to

$$K_{\mathrm{los,dB}} = 10 \log \frac{P_{\mathrm{LOS}}}{P_{\mathrm{SC}}} \tag{5.7}$$

where P_{LOS} is the power of the LOS component and P_{SC} is the power in the scattered MPCs.

If $K_{\mathrm{los,dB}}$ is above $0\,\mathrm{dB}$ the LOS component contains more power than all the scattered components together, hence good ranging should be possible. On the other hand the Ricean K-factor for the LOS component decreases if the distance between TX and RX increases, as the power in the LOS component decreases, while the power in the scattered components stays more or less the same. It also declines for NLOS scenarios, because the LOS component is heavily attenuated.

In Figure 5.15 the cdf of the Ricean K-factor for the LOS component can be seen. As expected have the NLOS BSs in both rooms a significantly lower $K_{\mathrm{los,dB}}$ than the LOS measurements. In room i10, the values are slightly higher because the room dimensions are not as big as in room i2, hence the distances between TX and RX are smaller.

In Figure 5.16 the absolute value of the ranging error as a function of $K_{\mathrm{los,dB}}$ is plotted. In both subplots a correlation between $K_{\mathrm{los,dB}}$ and the absolute value of the ranging error can be seen. Especially for $K_{\mathrm{los,dB}}$ values smaller than $-15\,\mathrm{dB}$ the ranging error increases. Unfortunately, too few measurements have been made, to get a reliable correlation func-

(a) i2　　　　　　　　　　　　　　(b) i10
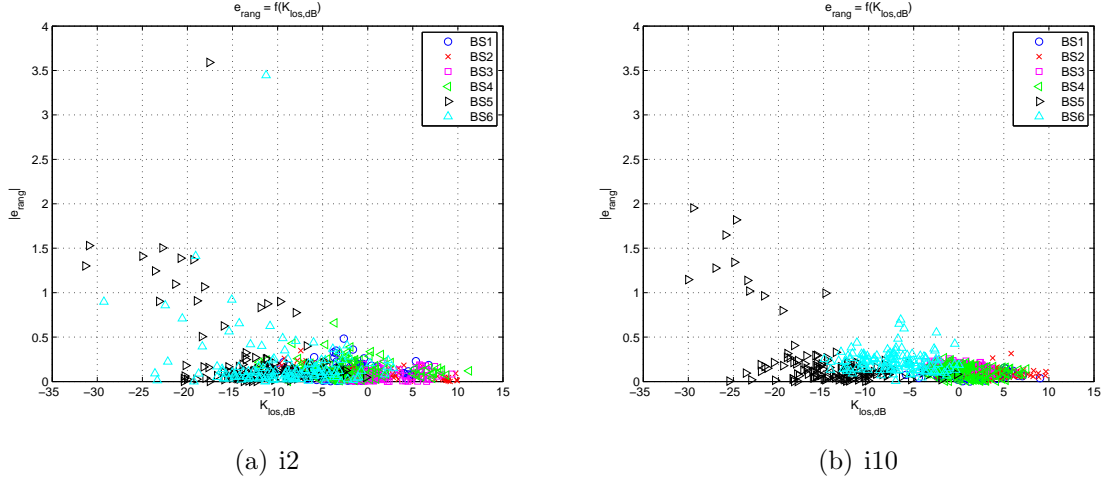
Figure 5.16: $|e_{\text{rang}}| = f(K_{\text{los,dB}})$

tion between these two variables.

5.3.4　Reverberation Distance

In analogy to Sabine's equation for the reverberation time for room acoustics, [ANP$^+$07] have developed a framework to calculate a reverberation distance for the electromagnetic field. Due to the assumptions that the diffuse field is only dependent on the volume, the surface area and an effective absorption coefficient, the power delay profiles of the diffuse field show an exponential decay. Moreover is it possible to calculate a reverberation distance r_{d}. For distances smaller than r_{d} the power of the deterministic components dominates the diffuse, randomly scattered power, whereas for larger distances the relation is inverted. As the derivation of the reverberation distance is quite long, only the most important results are presented, and the interested reader should refer to [ANP$^+$07] directly. The reverberation distance is

$$r_{\text{d}} = \frac{1}{2}\sqrt{D_{\text{TX}}D_{\text{RX}}A\mu} \tag{5.8}$$

where D_{TX} and D_{RX} are the directivities of the antennas, A is the absorption area and μ is the average absorption coefficient which can be expressed as

$$\mu = \frac{4V}{v_{\text{c}}A\tau} \tag{5.9}$$
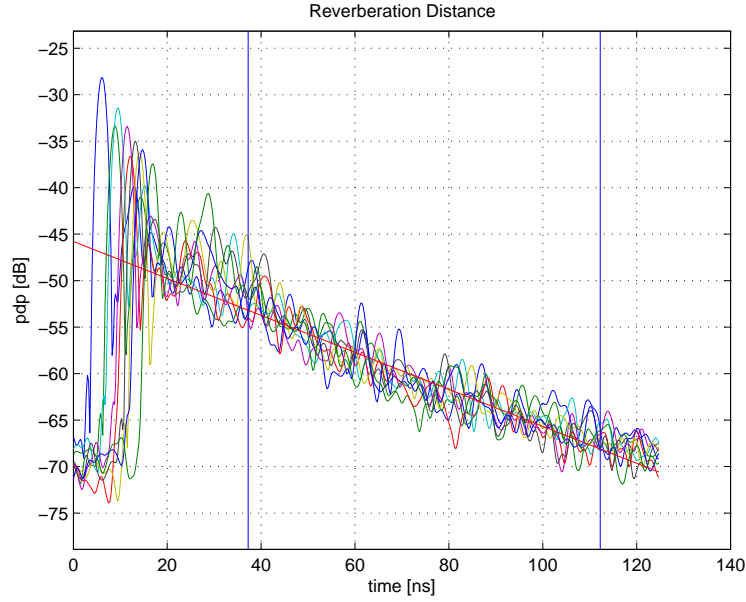
Figure 5.17: *pdp*'s for BS1 in Room i10

	τ in $[ns]$	μ	r_d in $[m]$
BS1	21.84	0.52	4.85
BS2	25.06	0.45	4.53
BS3	33.88	0.33	3.90
BS4	36.95	0.31	3.73
BS5	19.58	0.58	5.13
BS6	25.39	0.45	4.50

Table 5.8: Reverberation Distance and Model Parameters for Room i10

where V is the volume of the room, v_c is the speed of light and τ is the electromagnetic 'reverberation time'. In Figure 5.17 the power delay profiles of the nine positions for BS1 in room i10 can be seen. The red line shows the model which was gathered between the two blue lines, and has a decay rate of $0.20\,\mathrm{dB/ns}$. This decay rate corresponds to a reverberation time of $\tau = 21.84\,\mathrm{ns}$ and an average absorption coefficient of $\mu = 0.52$. From this follows a reverberation distance of $r_\mathrm{d} = 4.85\,\mathrm{m}$.

Although in [ANP+07] more measurements have been combined to gather the *pdp*s and hence a better average is obtained, it is still possible in Figure 5.17 to see, that the energy in the tail of the *pdp*s is not dependent on the distance between TX and RX.

In Table 5.8 the values for the reverberation distance for room i10 can be seen. The
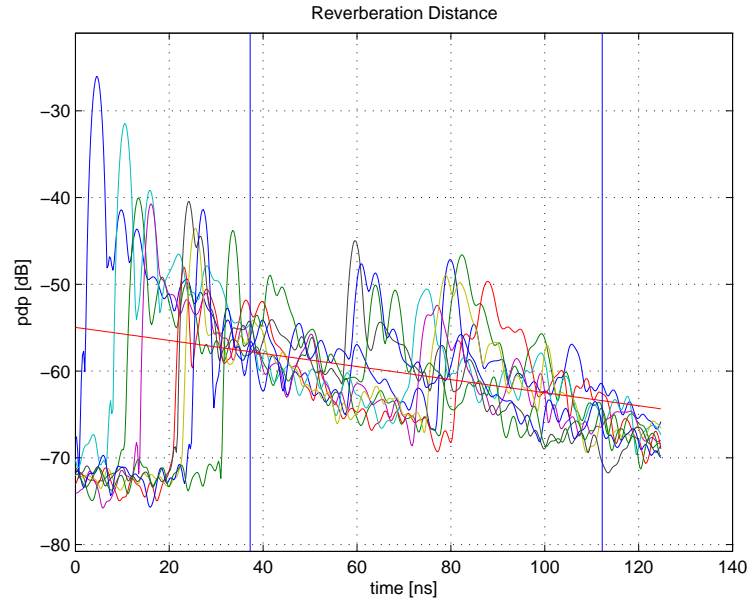
Figure 5.18: *pdp*'s for BS2 in Room i2

reverberation distance is for all the BSs in the same range. As explained above, the reverberation distance is not dependent whether the measurements have been performed with a LOS or not.

Due to the very late and strong reflections in room i2, which are depicted in Figure 5.18, it was difficult to set the limits of the model estimation, hence the reverberation distances for room i2 are not included in the thesis.

In the next chapter, the measurement results are fed into a positioning simulator to compare the obtained results and thus validate the simulator.

Chapter 6

Simulations with and Comparison to U-SPOT

In this chapter, the previously obtained CIRs are used in combination with the UWB System-Level Simulator for Positioning and Tracking (U-SPOT) which has been developed previously during a PhD Thesis [Gig10]. U-SPOT uses statistically defined environments chosen out of a measurement database. This measurement database is now filled with the measured LOS and NLOS CIRs and chooses a scenario out of the database according to pre-defined parameters.

The rest of the chapter is organized as follows: Section 6.1 briefly describes the simulation framework and Section 6.2 shows results obtained with the simulator as well as a comparison between the measured and simulated values to validate the simulator.

6.1   Framework of the Positioning Simulator U-SPOT

Figure 6.1 shows the structure of the positioning simulator. In this section only the main parts are described, and the interested reader is referred to [Gig10] and [GMPPW10] for further details.

For reasons of simulation speed U-SPOT works in complex baseband.

The scenario block defines the positions of the BSs and the TX. As tracking is not used in the simulations in Section 6.2 due to the fact that it is not possible to compare it to anything, the positions of the TX are chosen randomly. The simulator chooses randomly with respect to the overall probability of NLOS links p_{N}, the number of NLOS
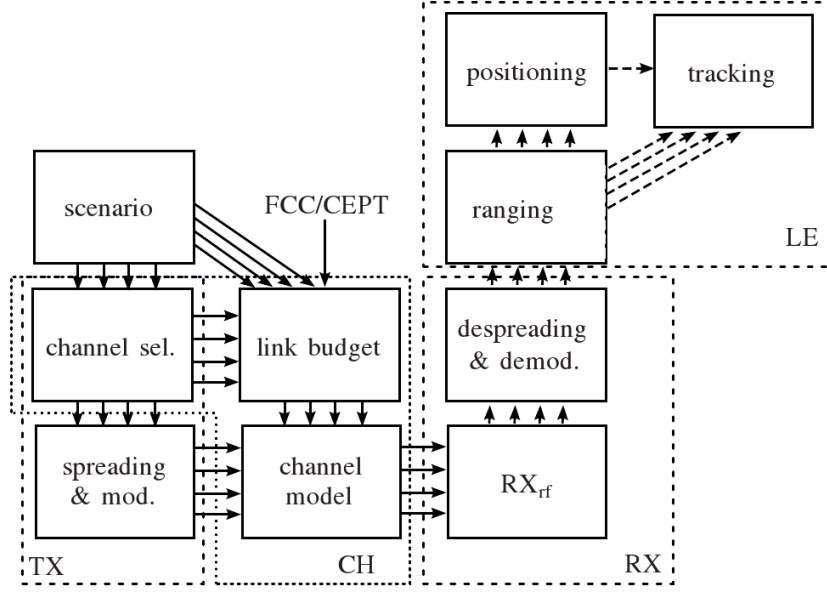
Figure 6.1: Structure of the positioning simulator [GMPPW10] (ⒸIEEE 2010)

N	$P_\mathrm{N}(0)$	$P_\mathrm{N}(0.25)$	$P_\mathrm{N}(0.5)$	Equation
0	1.00	0.316	0.063	$1 - p_\mathrm{N}^4$
1	0.00	0.422	0.250	$4p_\mathrm{N}(1 - p_\mathrm{N})^3$
2	0.00	0.211	0.375	$6p_\mathrm{N}^2(1 - p_\mathrm{N})^2$
3	0.00	0.047	0.250	$4p_\mathrm{N}^3(1 - p_\mathrm{N})$
4	0.00	0.004	0.063	p_N^4

Table 6.1: Probabilities for multiple NLOS links

links between the TX and the RXs according to Table 6.1 [Gig10], where N is the number of NLOS links, $P_\mathrm{N}(p_\mathrm{N})$ is the probability of N NLOS links and the last column describes the analytical equation for $P_\mathrm{N}(p_\mathrm{N})$.

The channel selection block picks a CIR out of the measured data. Each previously measured position[1] is now one measurement pool, hence in each room 60 LOS and 30 NLOS pools exist. The simulator now randomly chooses a pool and a CIR inside the pool.

Code Spreading and Modulation is done according to Equation 3.4.

Due to regulations in [IEE07b] and local regulations, the transmit energy E_p is limited. In [Gig10] a detailed analysis of the FCC/CEPT regulations for the IEEE 802.15.4a

---

[1]remember that each position consists of 15 measurements taken on a 3x5 grid (see Section 5.1)

standard is shown. The result of this analysis is an input signal-to-noise-ratio $\frac{E_{i,p}}{N_0}$ for the reference distance of $d_0 = 1\,\mathrm{m}$.

This input signal-to-noise-ratio for $1\,\mathrm{m}$ is then used to calculate the input SNR for the RXs at the receiving distance d_i by using the pathloss model

$$\frac{E_{i,p}}{N_0}(d_i, f_c)_{\mathrm{dB}} = \frac{E_{i,p}}{N_0}(d_0, f_c)_{\mathrm{dB}} - 10\eta \log \frac{d_i}{d_0} + S \tag{6.1}$$

according to [Gig10], where η is the pathloss exponent and S is a log-normal shadowing random variable with standard deviation σ_s. As one measurement pool is a small area, the large scale fading (LSF) is constant within one pool. The energy of the CIRs have been normalized to the mean of the respective measurement pool, hence small scale fading is inherent in the different CIRs. Now additive white Gaussian noise according to Equation 6.1 can be added to the received signal

$$r_{1,\mathrm{sim}}(t) = r_1(t) + \nu_{\mathrm{sim}}(t)$$

where $r_{1,\mathrm{sim}}(t)$ is the input for the RX in the simulator and $\nu_{\mathrm{sim}}(t)$ is artificial white Gaussian noise.

The RX in Figure 6.1 is either a high-performance coherent receiver or a low complexity energy detector. The coherent receiver is comparable to the RX structure developed in Section 3.2 as it also uses the repetitions of the preamble to get one CIR.

The ranging block also works with threshold-based ranging. To compare the measurement and the simulation results, the threshold has been set to the same value in both. As the optimal value for the parameter c in equation 4.2 which defines the threshold, lies between 0.1 and 0.15 for all BSs in both rooms, the parameter has been set to $c = 0.15$.

The positioning block also uses simple Least Squares estimation, as described in Section 4.2.

6.2 Results and Comparison

This part evaluates the U-SPOT simulator with the positioning results of Chapter 5.2.2. As the measurements are very time consuming, it would be nice to know how many measurements have to be made plus where the tag should be placed in a room to get

reliable results from the simulator. Therefore a scenario is defined to which the simulated values are compared to. This scenario consists of all measurement positions with a pre-defined threshold where the parameter c in Equation 4.2 is set to 0.15. The next parameter which has to be defined is the probability of NLOS links p_N. As comparisons to no, one and two NLOS links are possible with the measurement setup, p_N was set to 0 %, 25 % or 50 %.

To include the measured data in U-SPOT, the CIR, the pathloss exponent, the standard deviation of the log-normal shadowing variable and the LSF are needed. For each simulation scenario, these values differ and influence the simulations more or less significantly.

In Tables 6.2 to 6.7 the first rows always state the measured scenario, hence the comparison scenario. The second rows show the results of the simulation if all positions have been taken into account. For the third rows only the measurement positions 1, 3, 7 and 9 which presents the measurement positions in the four corners were used (cmp. Table 5.3 and Figure 5.3). The fourth rows only take the CIRs at grid position 8 into account, hence each measurement pool consists of only 1 measurement. In the last rows only measurement position 5 which lies in the middle of the room has been used, hence the LOS channel has four measurement pools and the NLOS channel has two.

The columns in these tables give the results for the CEP_{90}, the MAE and the standard deviation of the positioning error as well as the mean values and standard deviations for the errors in x- and y-direction.

The Figures 6.2 to 6.7 show the results graphically. The left subplots depict the cdf of the absolute positioning error and in the right subplots the position error with respect to the true position is plotted[2].

The simulation results in room i2 conform well with the measured scenario, especially for $p_N = 25\,\% \,\&\, 50\,\%$. While this is difficult to see in the tables, the cdf in the left subplots approve it very well. For the simulation scenario where only Position 5 was used, the positioning algorithm does not converge. This is due to the fact, that the parameters which are needed for simulations cannot be estimated correctly if only one position is measured. The other three simulation scenarios conform well with the measured data.

In room i10 the simulated scenarios perform worse than the measured scenario. This

---

[2]It is important to mention, that for better readability the limits for all the axes have been set to ± 0.8; thus some outliers are not included in the plot

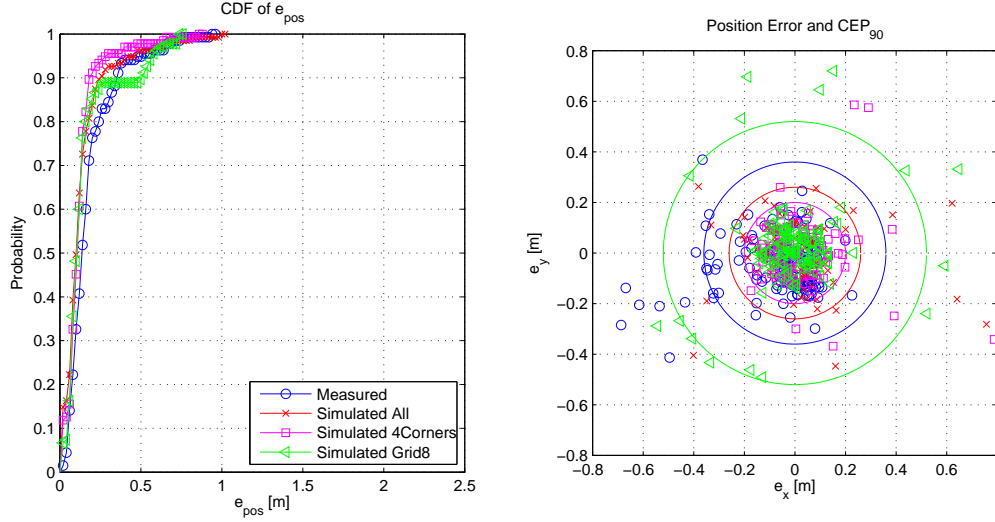| Scenario	CEP_{90}	MAE_{pos}	$\sigma_{\text{e}_{\text{pos}}}$	$\bar{e_{\text{x}}}$	$\sigma_{\text{e}_{\text{x}}}$	$\bar{e_{\text{y}}}$	$\sigma_{\text{e}_{\text{y}}}$
Measured	0.24	0.123	0.079	0.004	0.097	-0.001	0.110
Simu All	0.14	0.078	0.045	-0.010	0.063	-0.011	0.071
Simu 4Corners	0.16	0.080	0.055	0.014	0.071	-0.004	0.063
Simu Grid 8	0.16	0.089	0.045	-0.005	0.078	0.007	0.063
Simu Pos 5	NaN	10^{11}	10^{12}	10^{11}	10^{12}	10^{11}	10^{12}

Table 6.2: Positioning Results for Room i2 with $c = 0.15$: LOS $\rightarrow p_{\text{N}} = 0\,\%$
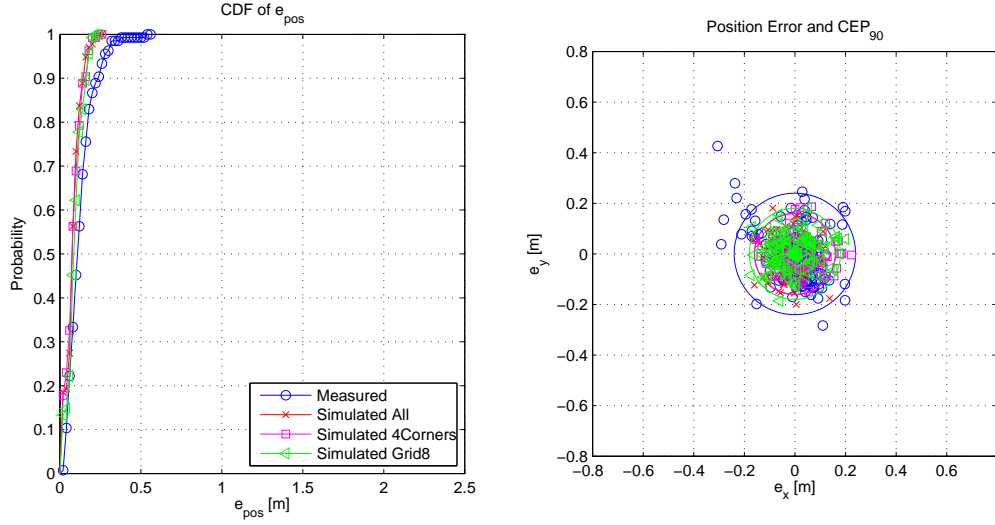
Figure 6.2: Comparison with $p_{\text{N}} = 0\,\%$ in Room i2

Scenario	CEP_{90}	MAE_{pos}	$\sigma_{\text{e}_{\text{pos}}}$	$\bar{e_{\text{x}}}$	$\sigma_{\text{e}_{\text{x}}}$	$\bar{e_{\text{y}}}$	$\sigma_{\text{e}_{\text{y}}}$
Measured	0.36	0.177	0.151	-0.076	0.181	-0.052	0.114
Simu All	0.24	0.135	0.148	-0.004	0.170	-0.002	0.110
Simu Corners	0.18	0.123	0.114	0.014	0.118	0.002	0.118
Simu Grid 8	0.51	0.153	0.164	-0.003	0.152	0.022	0.164
Simu Pos 5	NaN	10^{11}	10^{12}	10^{11}	10^{12}	10^{11}	10^{12}

Table 6.3: Positioning Results for Room i2 with $c = 0.15$: 1 NLOS $\rightarrow p_{\text{N}} = 25\,\%$

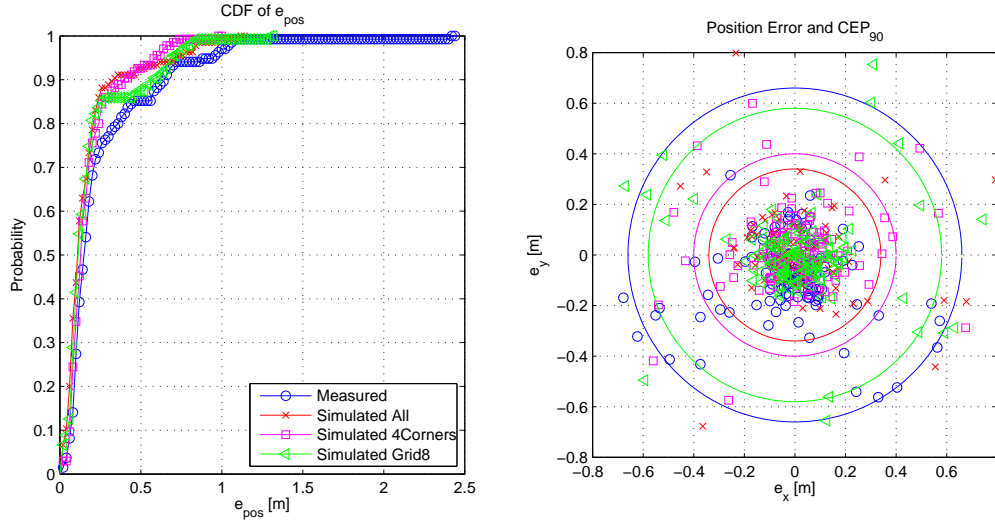| Scenario	CEP_{90}	MAE_{pos}	$\sigma_{\text{e}_{\text{pos}}}$	$\bar{e_{\text{x}}}$	$\sigma_{\text{e}_{\text{x}}}$	$\bar{e_{\text{y}}}$	$\sigma_{\text{e}_{\text{y}}}$
Measured	0.66	0.255	0.304	0.003	0.341	-0.098	0.180
Simu All	0.33	0.171	0.200	0.020	0.187	0.003	0.184
Simu Corners	0.39	0.180	0.164	0.001	0.192	0.018	0.148
Simu Grid 8	0.58	0.191	0.217	0.014	0.212	-0.019	0.195
Simu Pos 5	NaN	10^{11}	10^{12}	10^{11}	10^{12}	10^{11}	10^{12}

Table 6.4: Positioning Results for Room i2 with $c = 0.15$: 2 NLOS $\rightarrow p_{\text{N}} = 50\,\%$

Figure 6.3: Comparison with $p_N = 25\%$ in Room i2

Figure 6.4: Comparison with $p_N = 50\%$ in Room i2

Scenario	CEP_{90}	MAE_{pos}	$\sigma_{e_{pos}}$	$\bar{e}_x$	σ_{e_x}	$\bar{e}_y$	σ_{e_y}
Measured	0.10	0.051	0.028	-0.018	0.035	-0.009	0.043
Simu All	0.19	0.114	0.055	0.014	0.089	-0.002	0.095
Simu 4Corners	0.18	0.107	0.045	0.015	0.084	0.004	0.084
Simu Grid 8	0.18	0.105	0.045	0.006	0.089	-0.011	0.078
Simu Pos 5	0.18	0.111	0.055	-0.012	0.089	-0.007	0.084

Table 6.5: Positioning Results for Room i10 with $c = 0.15$: LOS $\rightarrow p_N = 0\%$
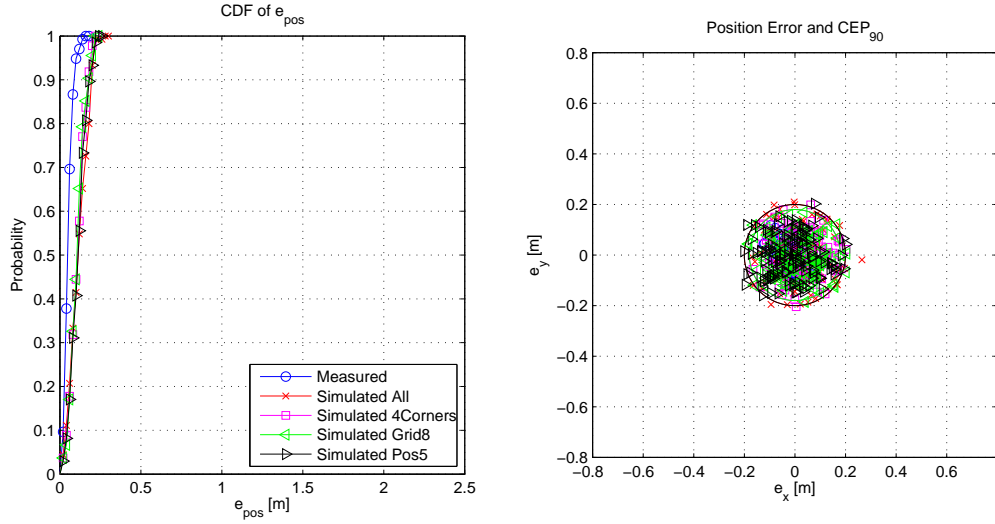
Figure 6.5: Comparison with $p_\mathrm{N} = 0\,\%$ in Room i10

Scenario	CEP_{90}	MAE_pos	σ_{e_pos}	$\bar{e_\mathrm{x}}$	σ_{e_x}	$\bar{e_\mathrm{y}}$	σ_{e_y}
Measured	0.48	0.143	0.252	0.053	0.186	-0.073	0.204
Simu All	0.22	0.139	0.118	-0.026	0.141	0.004	0.114
Simu 4Corners	0.27	0.176	0.237	-0.006	0.241	-0.005	0.170
Simu Grid 8	0.23	0.150	0.084	0.009	0.123	0.017	0.118
Simu Pos 5	0.33	0.170	0.148	-0.019	0.170	0.025	0.145

Table 6.6: Positioning Results for Room i10 with $c = 0.15$: 1 NLOS $\rightarrow p_\mathrm{N} = 25\,\%$
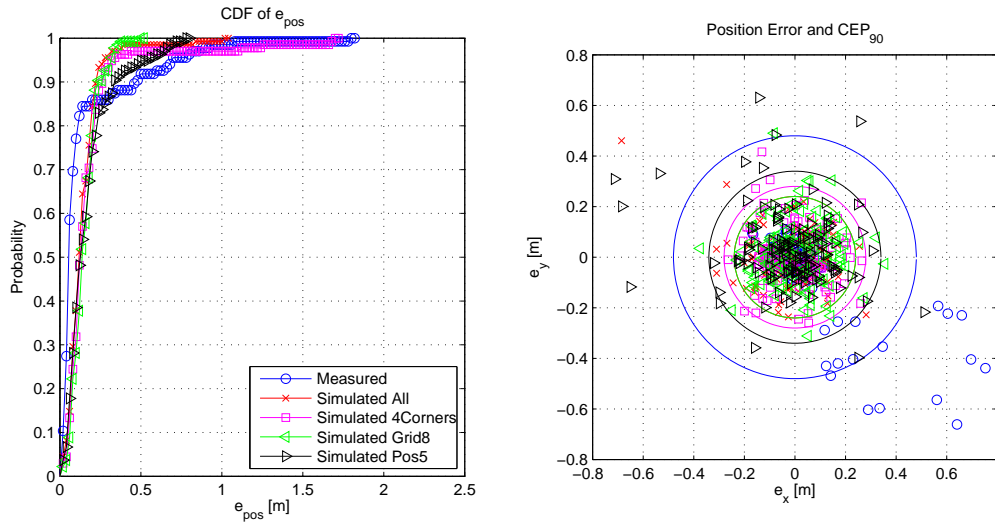
Figure 6.6: Comparison with $p_\mathrm{N} = 25\,\%$ in Room i10

Scenario	CEP_{90}	MAE_{pos}	$\sigma_{e_{\text{pos}}}$	$\bar{e}_{\text{x}}$	$\sigma_{e_{\text{x}}}$	$\bar{e}_{\text{y}}$	$\sigma_{e_{\text{y}}}$
Measured	0.46	0.167	0.250	0.081	0.225	-0.043	0.177
Simu All	0.35	0.212	0.268	-0.039	0.215	0.005	0.267
Simu 4Corners	0.42	0.226	0.217	0.007	0.226	-0.004	0.219
Simu Grid 8	0.29	0.150	0.084	-0.013	0.127	0.011	0.118
Simu Pos 5	0.34	0.172	0.141	0.010	0.158	-0.019	0.158

Table 6.7: Positioning Results for Room i10 with $c = 0.15$: 2 NLOS $\rightarrow p_{\text{N}} = 50\,\%$
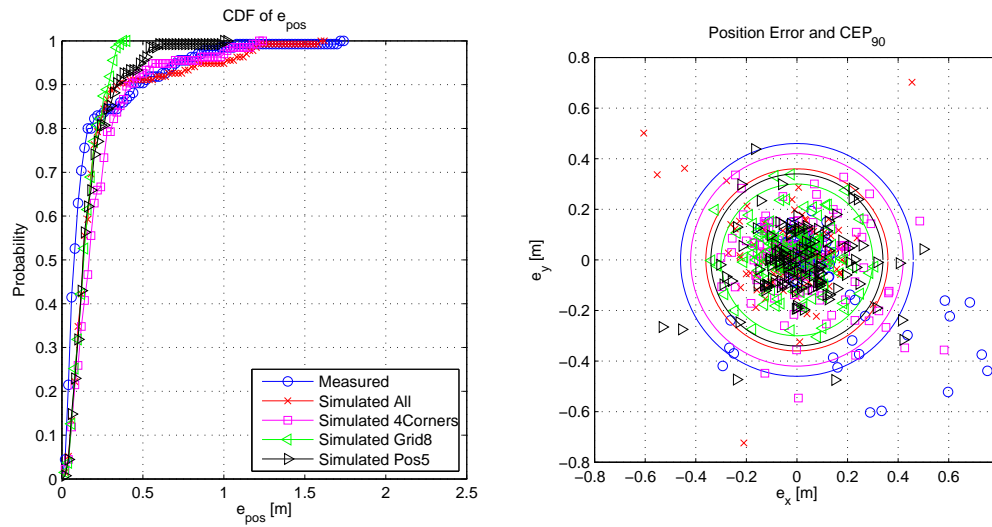
Figure 6.7: Comparison with $p_{\text{N}} = 50\,\%$ in Room i10

can be explained by the fact, that the estimated positions in the measurement scenario are too good (see Section 5.2.2). As U-SPOT uses the CIRs of all BSs for all simulated links, the misplacement of the BSs during the measurement appears.

Another possible reason for different results when simulated for $p_{N} = 25\%$ & 50% is the fact, that for the measurement always exactly one or two BSs had no LOS, respectively. In the simulation according to Table 6.1 there is the possibility, that zero to four NLOS links between the TX and the BSs occur.

To summarize this chapter, it can be said, that the simulation framework conforms well with the measured data. The best results are of course obtained, if all the CIRs are used for the simulator, but also for the simulations with only the four measurement positions in the corners of the room the results are qualitatively the same. If only measurement position 5 or grid position 8 is used, it cannot be guaranteed, that the simulations are trustworthy, due to the few measurements, and the possibly wrong estimated parameters.

Chapter 7

Conclusion and Further Work

In this section I will summarize the contribution of this thesis. Then I will conclude, by presenting the most important outcomes of it.

In the first part of this work the most important parts of the IEEE 802.15.4a standard that are needed for ranging have been presented. The synchronization header preamble of the UWB-PHY, especially the SYNC part are used for ranging purposes.

The next step to gather a range estimate between a TX and a RX has been to develop a coherent receiver structure for channel estimation. By applying undersampling the sampling frequency has been kept at an acceptable rate. However, due to this aliasing occurs. Hence the receiver structure for channel estimation has to be able to cope with that. It has been shown that it is possible to compute an estimation of the complex channel impulse response in baseband.

In an intense measurement campaign in two different rooms, a lecture hall and an office room, 1620 CIRs have been obtained. To estimate the range between the TX and the RX positions, simple threshold based leading edge detection has been performed. Due to multipath propagation, lots of reflections arrive at the RXs, especially in NLOS scenarios where the LOS component is not always the strongest one. Consequently a jump-back and search-forward algorithm has been applied to estimate the LOS and hence the distance between TX and RX. The CEP_{90} for ranging in LOS cases is always smaller than $26\,\mathrm{cm}$ and for NLOS measurements smaller than $88\,\mathrm{cm}$. Moreover have the most important parameters for multipath propagation been calculated to compare the two environments. The parameters of the two rooms are very comparable although the lecture hall is approximately twice as big as the office room.

Subsequently an iterative least-squares algorithm has been used to combine range estimates from different BSs to calculate the according position of the TX. In both measurement scenarios a CEP_{90} less than 60 cm is obtained with four range estimates where two of them have been taken from NLOS measurements.

In the last part of the work a comparison to the simulation framework U-SPOT [Gig10] has been presented to validate is. The simulator works qualitatively comparable to the real measurements if the previously measured CIRs are used as input.

Finally I want to present some topics which would be worthwhile to research further.

In Chapter 5.3 a connection between the Ricean K-factor for the LOS-component and the ranging error has been discovered. It would be interesting to investigate this correlation further and maybe find a mathematical description for it.

In this work, the trigger from the demonstrator is used to trigger the oscilloscope. To make a real implementation easier, the use of such a trigger could be avoided. By applying an energy detector and correlating the output with the template of the preamble it should be possible to find the beginning of an UWB frame. Then the solution presented in this work could be used.

As I did not know beforehand whether the positioning system would work with a sufficient accuracy in the two environments, which it certainly does, it would be interesting to max the system out, to obtain performance bounds. One way to do that would to take measurements in larger rooms, i.e. a industrial hall. On the other hand has the attenuation material been in the size of the wavelength, hence the wave bent around the object thus only mild NLOS links have been measured. Consequently measurements in an open-plan office with a separation between the individual work places would be interesting to investigate the influence of NLOS links even more.

Another possible measurement activity would be in a time-variant environment, where the tag is fixed to items which are moved in a room. Also the influence of people who block the LOS (this is probably the most realstic scenario) should be investigated.

All the before mentioned measurements could then be embedded into the simulation framework U-SPOT, to simulate different scenarios and validate the simulator even further.

As U-SPOT does not only analyse a coherent receiver structure, but also an energy detector, the implementation of such a receiver would be interesting. The already measured data could be used in a first step to compare the results.

Appendix A

Noise Analysis

This appendix presents the derivation of the Noise Analysis in Chapter 3.3. The input to the receiver is

$$r[n] = \nu[n]$$

where $\nu[n]$ is additive white gaussian noise with

$$\nu[n] \; iid \; \mathcal{N}(0, \sigma^2)$$

where iid means independent, identically distributed which means, that

$$E\{\nu[n]\nu[n+m]\} = 0 \quad \text{for} \quad m \neq 0$$

First the received signal is filtered with the reference pulse $rrc(t)$

$$r_{\mathrm{f}}[n] \sim \mathcal{N}(0, \sigma^2 \sum_k rrc^2[k]) \sim \mathcal{N}(0, \sigma^2)$$

since

$$\sum_k rrc^2[k] = 1$$

The signal $r_{\mathrm{f}}[n]$ is now no longer iid, however

$$E\{r_{\mathrm{f}}[n]r_{\mathrm{f}}[n+i]\} = 0 \quad \text{if } |i| \geq N_{\mathrm{f}}$$

where N_f is the filter order. Zero-Padding in the frequency domain does only add zeros to the Fourier transform of the signal (see Figure 3.7) and hence also only adds zeros to the power spectral density (PSD) of the signal. Due to the fact that the variance is the integration of the PSD normalized by the sampling frequency, the variance of the signal is not changed by zero-padding.

$$r_\mathrm{f}[m] \sim \mathcal{N}(0, \sigma^2)$$

The next step in the estimation of the CIR is to shift the signal in the frequency domain by $\hat{f}_\mathrm{c,low}$, sum up over the repetitions of the preamble and seperate real and imaginary part. The real part of $\boldsymbol{q}[k]$ is therefore

$$\mathrm{Re}\{q[k]\} = \sum_{l=1}^{N_\mathrm{sync}-1} r_\mathrm{f}[k + lN'_\mathrm{1pr}] \cos(2\pi \hat{f}_\mathrm{c,low} T'_\mathrm{s}[k + lN'_\mathrm{1pr}])$$

The mean value follows as

$$\mathrm{E}\{\mathrm{Re}\{q[k]\}\} = \mathrm{E}\left\{ \sum_{l=1}^{N_\mathrm{sync}-1} r_\mathrm{f}[k + lN'_\mathrm{1pr}] \cos(2\pi \hat{f}_\mathrm{c,low} T'_\mathrm{s}[k + lN'_\mathrm{1pr}]) \right\}$$

$$= \sum_{l=1}^{N_\mathrm{sync}-1} \mathrm{E}\left\{ r_\mathrm{f}[k + lN'_\mathrm{1pr}] \cos(2\pi \hat{f}_\mathrm{c,low} T'_\mathrm{s}[k + lN'_\mathrm{1pr}]) \right\} = 0$$

since $r_\mathrm{f}[m]$ is zero-mean. The variance of $\boldsymbol{q}[k]$ can be calculated as

$$\mathrm{var}\{\mathrm{Re}\{q[k]\}\} = \mathrm{E}\left\{ (\sum_{l=1}^{N_\mathrm{sync}-1} r_\mathrm{f}[k + lN'_\mathrm{1pr}] \cos(2\pi \hat{f}_\mathrm{c,low} T'_\mathrm{s}[k + lN'_\mathrm{1pr}]))^2 \right\}$$

$$= \mathrm{E}\left\{ \sum_{l=1}^{N_\mathrm{sync}-1} r_\mathrm{f}[k + lN'_\mathrm{1pr}] \cos(2\pi \hat{f}_\mathrm{c,low} T'_\mathrm{s}[k + lN'_\mathrm{1pr}]) \right.$$

$$\left. \sum_{v=1}^{N_\mathrm{sync}-1} r_\mathrm{f}[k + vN'_\mathrm{1pr}] \cos(2\pi \hat{f}_\mathrm{c,low} T'_\mathrm{s}[k + vN'_\mathrm{1pr}]) \right\}.$$

if $\quad l \neq v \rightarrow \mathrm{E}\{r_\mathrm{f}[k + lN'_\mathrm{1pr}]r_\mathrm{f}[k + vN'_\mathrm{1pr}]\} = 0$, hence

$$\mathrm{var}\{\mathrm{Re}\{q[k]\}\} = \sum_{l=1}^{N_\mathrm{sync}-1} \mathrm{E}\{r_\mathrm{f}^2[k + lN'_\mathrm{1pr}]\} \cos^2(2\pi \hat{f}_\mathrm{c,low} T'_\mathrm{s}[k + lN'_\mathrm{1pr}])$$

$$= \sigma^2 \sum_{l=1}^{N_\mathrm{sync}-1} \cos^2(2\pi \hat{f}_\mathrm{c,low} T'_\mathrm{s}[k + lN'_\mathrm{1pr}])$$

$$= \sigma^2_\mathrm{sum,1}[k].$$

This holds true if

$$N'_\mathrm{1pr} \geq N_\mathrm{f} \tag{A.1}$$

The same holds true for the imaginary part of $q[k]$, only that the cosine is a sine. Hence

$$q[k] \sim \begin{cases} \mathcal{N}(0, \sigma^2_\mathrm{sum,1}[k]) \\ \mathcal{N}(0, \sigma^2_\mathrm{sum,2}[k]) \end{cases}$$

where both, the real and imaginary part are again uncorrelated for $|i| \geq N_\mathrm{f}$. Moreover are the real- and imaginary part of $q[k]$ now correlated

$$\mathrm{E}\{\mathrm{Re}\{q[k]\} \, \mathrm{Im}\{q[k]\}\} =$$

$$= \mathrm{E}\Bigg\{ \sum_{l=1}^{N_\mathrm{sync}-1} r_\mathrm{f}[k + lN'_\mathrm{1pr}] \cos(2\pi \hat{f}_\mathrm{c,low} T'_\mathrm{s}[k + lN'_\mathrm{1pr}])$$

$$\sum_{v=1}^{N_\mathrm{sync}-1} r_\mathrm{f}[k + vN'_\mathrm{1pr}] \sin(2\pi \hat{f}_\mathrm{c,low} T'_\mathrm{s}[k + vN'_\mathrm{1pr}]) \Bigg\}$$

if $\quad l \neq v \rightarrow \mathrm{E}\{r_\mathrm{f}[k + lN'_\mathrm{1pr}]r_\mathrm{f}[k + vN'_\mathrm{1pr}]\} = 0$

$$= \sigma^2 \sum_{l=1}^{N_\mathrm{sync}-1} \cos(2\pi \hat{f}_\mathrm{c,low} T'_\mathrm{s}[k + lN'_\mathrm{1pr}]) \sin(2\pi \hat{f}_\mathrm{c,low} T'_\mathrm{s}[k + lN'_\mathrm{1pr}])$$

$$= \sigma^2_\mathrm{cos,sin}[k].$$

This is the inner product of two orthogonal functions, hence low correlation is expected.

The next step is the matrix multiplication with the inverse of $\boldsymbol{C}[k]$.

$$\begin{bmatrix} a_{\mathrm{f}}[k] \\ b_{\mathrm{f}}[k] \end{bmatrix} = 2\boldsymbol{C}^{-1}[k]\boldsymbol{q}[k] = 2 \begin{bmatrix} c_{11}[k] & c_{12}[k] \\ c_{21}[k] & c_{22}[k] \end{bmatrix} \begin{bmatrix} \mathrm{Re}\{\boldsymbol{q}[k]\} \\ \mathrm{Im}\{\boldsymbol{q}[k]\} \end{bmatrix}$$

The mean and the variance of $a_{\mathrm{f}}[k]$ and $b_{\mathrm{f}}[k]$ can then be calculated to

$$\mathrm{E}\{a_{\mathrm{f}}[k]\} = \mathrm{E}\{2c_{11}[k]\mathrm{Re}\{\boldsymbol{q}[k]\} + 2c_{12}[k]\mathrm{Im}\{\boldsymbol{q}[k]\}\} = 0$$

$$\begin{aligned} \mathrm{var}\{a_{\mathrm{f}}[k]\} &= \mathrm{E}\big\{(2c_{11}[k]\mathrm{Re}\{\boldsymbol{q}[k]\} + 2c_{12}[k]\mathrm{Im}\{\boldsymbol{q}[k]\})^2\big\} \\ &= 4c_{11}^2[k]\sigma_{\mathrm{sum},1}^2[k] + 4c_{12}^2[k]\sigma_{\mathrm{sum},2}^2[k] + 8c_{11}[k]c_{12}[k]\sigma_{\mathrm{cos,sin}}^2[k] \\ &= \sigma_{\mathrm{C},1}^2[k] \end{aligned}$$

$$\mathrm{E}\{b_{\mathrm{f}}[k]\} = \mathrm{E}\{2c_{21}[k]\mathrm{Re}\{\boldsymbol{q}[k]\} + 2c_{22}[k]\mathrm{Im}\{\boldsymbol{q}[k]\}\} = 0$$

$$\begin{aligned} \mathrm{var}\{b_{\mathrm{f}}[k]\} &= \mathrm{E}\big\{(2c_{21}[k]\mathrm{Re}\{\boldsymbol{q}[k]\} + 2c_{22}[k]\mathrm{Im}\{\boldsymbol{q}[k]\})^2\big\} \\ &= 4c_{21}^2[k]\sigma_{\mathrm{sum},1}^2[k] + 4c_{22}^2[k]\sigma_{\mathrm{sum},2}^2[k] + 8c_{21}[k]c_{22}[k]\sigma_{\mathrm{cos,sin}}^2[k] \\ &= \sigma_{\mathrm{C},2}^2[k] \end{aligned}$$

where both variables, $a_{\mathrm{f}}[k]$ and $b_{\mathrm{f}}[k]$ are again uncorrelated if $|i| \geq N_{\mathrm{f}}$. The final step towards the estimated channel impulse response is despreading. This is described as

$$\hat{h}[k] = \frac{2}{M_1} \sum_{i=0}^{N_{\mathrm{code}}-1} (a_{\mathrm{f}}[k + iN_{\mathrm{c}}'] + jb_{\mathrm{f}}[k + iN_{\mathrm{c}}'])c_6[i]$$

The derivation of the mean of $\hat{h}[k]$ is straightforward

$$\begin{aligned} \mathrm{E}\big\{\hat{h}[k]\big\} &= \mathrm{E}\left\{\frac{2}{M_1} \sum_{w=1}^{N_{\mathrm{code}}-1} (a_{\mathrm{f}}[k + wN_{\mathrm{c}}'] + jb_{\mathrm{f}}[k + wN_{\mathrm{c}}'])c_6[i]\right\} \\ &= \frac{2}{M_1} \sum_{w=1}^{N_{\mathrm{code}}-1} \mathrm{E}\{(a_{\mathrm{f}}[k + wN_{\mathrm{c}}'] + jb_{\mathrm{f}}[k + wN_{\mathrm{c}}'])c_6[i]\} = 0 \end{aligned}$$

since $a_{\mathrm{f}}[k]$ and $b_{\mathrm{f}}[k]$ are zero-mean.

The variance of the real part of $\hat{h}[k]$ can be calculated in the following way:

$$\mathrm{var}\Big\{\mathrm{Re}\big\{\hat{h}[k]\big\}\Big\} = \mathrm{E}\left\{ (\frac{2}{M_1} \sum_{w=1}^{N_{\mathrm{code}}-1} a_{\mathrm{f}}[k+wN_{\mathrm{c}}']c_6[i])^2 \right\}$$

$$= \mathrm{E}\left\{ \frac{2}{M_1} \sum_{w=1}^{N_{\mathrm{code}}-1} a_{\mathrm{f}}[k+wN_{\mathrm{c}}']c_6[i] \right.$$

$$\left. \frac{2}{M_1} \sum_{z=1}^{N_{\mathrm{code}}-1} a_{\mathrm{f}}[k+zN_{\mathrm{c}}']c_6[i] \right\},$$

if $w \neq z \quad \mathrm{E}\{a_{\mathrm{f}}[k+wN_{\mathrm{c}}']a_{\mathrm{f}}[k+zN_{\mathrm{c}}']\} = 0$

$$\mathrm{var}\Big\{\mathrm{Re}\big\{\hat{h}[k]\big\}\Big\} = \frac{4}{M_1^2} \sum_{w=1}^{N_{\mathrm{code}}-1} \mathrm{E}\{\sigma_{\mathrm{C},1}^2[k+wN_{\mathrm{c}}']c_6[i]\}$$

$$= \sigma_{\mathrm{h}_1}^2[k]$$

This holds only true if

$$N_{\mathrm{c}}' \geq N_{\mathrm{f}} \tag{A.2}$$

Now two conditions for the filter order N_{f} exist: Equation A.1 and A.2. Since the second one is more strict Equation A.2 is used to get a bound for N_{f}.

$$N_{\mathrm{f}} \leq N_{\mathrm{c}}' = LT\mathrm{chip}f_{\mathrm{s}}' \tag{A.3}$$

By applying the same derivation to the imaginary part, the estimated channel impulse response shows the following distribution:

$$\begin{bmatrix} \mathrm{Re}\big\{\hat{h}[k]\big\} \\ \mathrm{Im}\big\{\hat{h}[k]\big\} \end{bmatrix} \sim \begin{bmatrix} \mathcal{N}(0, \sigma_{\mathrm{h}_1}^2[k]) \\ \mathcal{N}(0, \sigma_{\mathrm{h}_2}^2[k]) \end{bmatrix}$$

Appendix B

Measurement Equipment

The measurement setup is depicted in Figure 5.1. The used equipment in Tables 5.1 and 5.2 is:

- Demonstrator: [Gig10], [Buc08]

- High Pass Filter:

    - Mini Circuits: VHP 26
    - HPF developed by TU Vienna

- Low Noise Amplifier:

    - Narda West: DBS 0208N315
    - Miteq: JS4-00101200-30-10P-C1

- Antenna:

    - Skycross: 222-1137C
    - 5-Cent Antenna: [Kra08]

- Oscilloscope: Agilent Infiniium 54855A

- pyramidal absorber for NLOS measurements: Telemeter Electronic EPP12

Bibliography

[ANP⁺07]   J.B. Andersen, J.O. Nielsen, G.F. Pedersen, G. Bauch, and M. Herdin. Room electromagnetics. *Antennas and Propagation Magazine, IEEE*, 49(2):27 –33, april 2007.

[AVO99]   John R. Buck Alan V. Oppenheim, Ronald W. Schafer. *Discrete-Time Signal Processing.* Prentice Hall, 2 edition, 1999.

[Buc08]   Thomas Buchgraber. Experimental evaluation of the IEEE 802.15.4a standard. Master's thesis, Institute for Signal Processing and Speech Communication, Graz University of Technology, 2008.

[DCF⁺09]   D. Dardari, A. Conti, U. Ferner, A. Giorgetti, and M.Z. Win. Ranging with ultrawide bandwidth signals in multipath environments. *Proceedings of the IEEE*, 97(2):404 –426, feb. 2009.

[DW07]   V. Dizdarevic and K. Witrisal. Statistical UWB range error model for the threshold leading edge detector. In *Information, Communications Signal Processing, 2007 6th International Conference on*, pages 1 –5, dec. 2007.

[GBA⁺09]   T. Gigl, T. Buchgraber, A. Adalan, J. Preishuber-Pfluegl, M. Fischer, and K. Witrisal. UWB channel characterization using IEEE 802.15.4a demonstrator system. In *Ultra-Wideband, 2009. ICUWB 2009. IEEE International Conference on*, pages 230 –234, sept. 2009.

[Gei09]   Bernhard Geiger. Enhanced Accuracy Channel Estimation and Ranging for Energy Detectors. Master's thesis, Institute for Signal Processing and Speech Communication, Graz University of Technology, 2009.

[Gig10]   Thomas Gigl. *Low-Complexity Localization using Standard-Compliant UWB Signals.* PhD thesis, Institute for Signal Processing and Speech Communication, Graz University of Technology, 2010.

[GMPPW10] T. Gigl, P. Meissner, J. Preishuber-Pfluegl, and K. Witrisal. Ultra-wideband system-level simulator for positioning and tracking (U-SPOT). In *Indoor Positioning and Indoor Navigation (IPIN), 2010 International Conference on*, pages 1 –9, sept. 2010.

[Ham83]   Richard W. Hamming. *Digitale Filter.* 2 edition, 1983.

[IEE06]   Standard Organisation IEEE. Part 15.4: Wireless Medium Access Control (MAC) and Physical Layer (PHY) Specifications for Low-Rate Wireless Personal Area Networks (WPANs). 2006.

[IEE07a]   Standard Organisation IEEE. Part 11: Wireless LAN Medium Access Control (MAC) and Physical Layer (PHY) Specifications. 2007.

[IEE07b]   Standard Organisation IEEE. Part 15.4: Wireless Medium Access Control (MAC) and Physical Layer (PHY) Specifications for Low-Rate Wireless Personal Area Networks (WPANs),Amendment 1: Add Alternate PHYs. 2007.

[IJN⁺06]   Z. Irahhauten, G.J.M. Janssen, H. Nikookar, A. Yarovoy, and L.P. Ligthart. UWB channel measurements and results for office and industrial environments. In *Ultra-Wideband, The 2006 IEEE 2006 International Conference on*, pages 225 –230, sept. 2006.

[Kay88]   Steven M. Kay. *Modern Spectral Estimation.* 1988.

[Kra08]   C. Krall. *Signal Processing for Ultra Wideband Transceivers.* PhD thesis, Institute for Signal Processing and Speech Communication, Graz University of Technology, 2008.

[Pro01]   John G. Proakis. *Digital Communications.* 4th edition, 2001.

[Rap01]   Theodore S. Rappaport. *Wireless Communications: Principles and Practice.* Prentice Hall PTR, 2001.

[Sha98]   C.E. Shannon. Communication in the presence of noise. *Proceedings of the IEEE*, 86(2):447 –457, feb 1998.

[Til10]   Johannes Benjamin Till. Positioning methods using energy detectors in IEEE 802.15.4a-UWB. Master's thesis, Institute for Signal Processing and Speech Communication, Graz University of Technology, 2010.

[ZS08]   I. Guvenc Z. Sahinoglu, S. Gezici. *Ultra-wideband Positioning Systems*. 2008.